A Nuclear Role for miR-9 and Argonaute Proteins in Balancing Quiescent and Activated Neural Stem Cell States

Shauna Katz, Delphine Cussigh, Noelia Urbán, Isabelle Maria Blomfield, François Guillemot, Laure Bally-Cuif, Marion Coolen

Article

Cell Reports

A Nuclear Role for miR-9 and Argonaute Proteins in Balancing Quiescent and Activated Neural Stem Cell States

Graphical Abstract

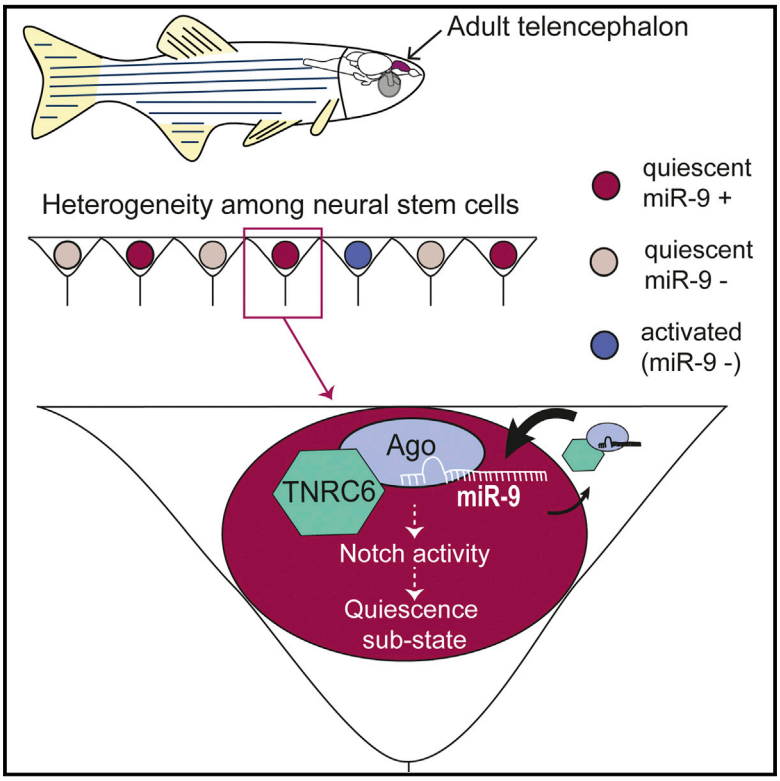

Highlights

- miR-9 highlights a state heterogeneity among adult quiescent neural stem cells (NSC)
- miR-9 maintains NSC quiescence notably through permitting efficient Notch signaling
- miR-9, along with Argonaute proteins, is present in the nucleus of adult quiescent NSCs
- Active nucleo-cytoplasmic shuttling of miR-9/Ago impacts NSCs quiescence status

Authors

Shauna Katz, Delphine Cussigh, Noelia Urbán, Isabelle Blomfield, François Guillemot, Laure Bally-Cuif, Marion Coolen

Correspondence

laure.bally-cuif@pasteur.fr (L.B.-C.), marion.coolen@pasteur.fr (M.C.)

In Brief

An essential protective feature of adult neural stem cells is their relative quiescence. Katz et al. identify microRNA-9 as crucial factor that maintains adult NSCs quiescence and sets a heterogeneity within these cells, through a non-canonical nuclear mode of action.

Katz et al., 2016, Cell Reports *17*, 1383–1398
October 25, 2016
http://dx.doi.org/10.1016/j.celrep.2016.09.088

Cell Reports
Article

A Nuclear Role for miR-9 and Argonaute Proteins in Balancing Quiescent and Activated Neural Stem Cell States

Shauna Katz,[1] Delphine Cussigh,[1,2] Noelia Urbán,[3] Isabelle Blomfield,[3] François Guillemot,[3] Laure Bally-Cuif,[1,2,4,*] and Marion Coolen[1,2,*]
[1]Zebrafish Neurogenetics Group, Paris-Saclay Institute of Neuroscience (Neuro-PSI), UMR 9197, CNRS-University Paris-Sud, Avenue de la Terrasse, 91190 Gif-sur-Yvette, France
[2]Department of Developmental and Stem Cell Biology, Institut Pasteur and CNRS UMR 3738, 25 rue du Dr Roux, 75015 Paris, France
[3]Mill Hill Laboratory, The Francis Crick Institute, The Ridgeway, Mill Hill, London NW7 1AA, UK
[4]Lead Contact
*Correspondence: laure.bally-cuif@pasteur.fr (L.B.-C.), marion.coolen@pasteur.fr (M.C.)
http://dx.doi.org/10.1016/j.celrep.2016.09.088

SUMMARY

Throughout life, adult neural stem cells (NSCs) produce new neurons and glia that contribute to crucial brain functions. Quiescence is an essential protective feature of adult NSCs; however, the establishment and maintenance of this state remain poorly understood. We demonstrate that in the adult zebrafish pallium, the brain-enriched miR-9 is expressed exclusively in a subset of quiescent NSCs, highlighting a heterogeneity within these cells, and is necessary to maintain NSC quiescence. Strikingly, miR-9, along with Argonaute proteins (Agos), is localized to the nucleus of quiescent NSCs, and manipulating their nuclear/cytoplasmic ratio impacts quiescence. Mechanistically, miR-9 permits efficient Notch signaling to promote quiescence, and we identify the RISC protein TNRC6 as a mediator of miR-9/Agos nuclear localization in vivo. We propose a conserved non-canonical role for nuclear miR-9/Agos in controlling the balance between NSC quiescence and activation, a key step in maintaining adult germinal pools.

INTRODUCTION

Resident neural stem cells (NSCs) in the adult brain produce new neurons and glia and display two fundamental features: multipotency and long-term self-renewal capacity. Characterization of the adult neurogenesis process has shed light on the importance of accurate NSCs control in brain homeostasis, behavior, and brain repair/regeneration (Lim and Alvarez-Buylla, 2014; Ming and Song, 2011). In the adult mouse brain, NSCs are found primarily in two microenvironmental niches located in the telencephalon: the subependymal zone (SEZ) of the lateral ventricle and the subgranular zone (SGZ) of the dentate gyrus of the hippocampus (Lim and Alvarez-Buylla, 2014). By contrast, in the zebrafish, which is emerging as an attractive comparative model, widespread neurogenesis is maintained at adult stages in several brain regions (Adolf et al., 2006; Grandel et al., 2006), including the dorsal telencephalon (or pallium), which encompasses areas homologous to the rodent SEZ and SGZ (Dirian et al., 2014). In this region, radial glia cells (RG), constituting a large population that lines the surface of the brain ventricle, have been identified as NSCs (Figures S1A and S1B). These cells share features with NSCs found in the mammalian brain including their radial morphology, the expression of astroglial markers (GFAP, GS, BLBP), and neurogenic stem cell markers (Sox2, Nestin, Msi1, and the zebrafish *Hes5* ortholog, *her4*) (Chapouton et al., 2010; Ganz et al., 2010; März et al., 2010; Alunni et al., 2013; Dirian et al., 2014; Than-Trong and Bally-Cuif, 2015). Lineage tracing and clonal analyses have revealed that these NSCs contribute to constitutive adult neurogenesis and are able to self-renew and give rise to functional neurons at the single cell level, both qualifying them as genuine stem cells and demonstrating their robust neurogenic activity (Kroehne et al., 2011; Rothenaigner et al., 2011).

A distinguishing feature of adult NSCs when compared with embryonic neural progenitor cells (NPCs), both in zebrafish and mammals, is their relative quiescence. Quiescence is a reversible state of cell-cycle arrest, which is actively maintained and involves profound alterations in cell physiology (Cheung and Rando, 2013). Disrupting the balance between quiescent and activated NSCs leads to a premature depletion or silencing of long-lasting NSCs (Codega et al., 2014; Encinas et al., 2011; Hsieh, 2012). Some key signaling or cell-cell interaction pathways, notably Notch and TGFβ/BMP (Giachino and Taylor, 2014), have been identified in maintaining quiescence. In particular, in the zebrafish adult pallium, inhibiting Notch signaling leads the entire population of NSCs to enter the cell cycle (Alunni et al., 2013). Recent works further demonstrated that quiescent NSCs are heterogeneous in their activation potential, their reactivity to various stimuli and, once activated, their division rate and ability to re-enter into quiescence (Hsieh, 2012; Lugert et al., 2010). However, how quiescence cues are integrated to establish this cell state and the diversity within it have yet to be assessed.

MicroRNAs are small regulatory RNAs that are known to post-transcriptionally regulate gene expression via complementary base pairing with mRNA targets (Bartel, 2009). Canonical microRNA genes are transcribed into primary transcripts (pri-miRs) containing a hairpin structure, which is cleaved out by the nuclear microprocessor complex to give rise to a precursor microRNA (pre-miR). Exportin 5 transports the pre-miR to the cytoplasm where the RNase III enzyme Dicer processes it into a mature microRNA duplex. The duplex is subsequently unwound, and one strand is preferentially integrated into the RNA-induced silencing complex (RISC), which guides it to mRNA targets. The RISC is most notably composed of one Argonaute (Ago) effector protein, inside which the microRNA strand is loaded, and one GW182 protein (or TNRC6), which mediates downstream steps in the cascade of microRNA-mediated gene regulation (Meister, 2013). Because microRNAs can potentially regulate hundreds of mRNA targets, they are generally thought of as fine-tuners of gene expression, buffering or reinforcing developmental and transitional states. Additionally, microRNA levels and functions are influenced by both cell extrinsic and intrinsic signals (Nam et al., 2014; Rissland et al., 2011). As such, microRNAs are attractive candidates for integrating environmental and internal cues in the regulation of NSCs quiescence/activation balance.

MicroRNA-9 (miR-9) is a highly conserved neural microRNA, shown to be a determinant regulator of NPCs during vertebrate embryonic development (Coolen et al., 2013). Expression of miR-9-5p (the preferred mature strand in vertebrate embryos, henceforth referred to simply as miR-9) is enriched to NPCs and committed neuronal precursors in the proliferative ventricular zone (VZ); it promotes the transition of NPCs from a proliferative to a neurogenic mode and is crucial in the timing of their cell-cycle exit (Leucht et al., 2008; Bonev et al., 2011; Shibata et al., 2011; Coolen et al., 2012). Studies performed on mouse NSCs proliferating in vitro also suggested that it could play a similar role in adult NSCs dynamics (Zhao et al., 2009). To challenge this hypothesis in a physiological context in which adult NSCs are mostly quiescent, we assessed here the role of miR-9 in adult zebrafish NSCs in vivo. We show that miR-9 expression highlights a sub-state within the quiescence phase of adult NSCs, and we demonstrate that it maintains quiescence through potentiating Notch signaling activity. Remarkably, we also find that miR-9 controls this key stem cell property via a non-canonical nuclear mechanism.

RESULTS

miR-9 Is Expressed Exclusively in Quiescent Neural Stem Cells in the Adult Telencephalon

To determine whether miR-9 could also control transitional states in neural progenitors at late stages, we first assessed the expression of the seven primary transcripts encoding miR-9 (pri-miR-9) in embryonic, juvenile, and adult zebrafish brains using qRT-PCR. We could detect the seven pri-miR-9 transcripts at all stages. However, there was a progressive change in the respective contribution of the different transcripts to the total pri-miR-9 pool (Figure 1A). We found that pri-miR-9-6 is the most predominantly expressed miR-9 transcript in the adult brain, in contrast to the situation in the embryo, where pri-miR-9-2 is the most highly expressed. In situ hybridization (ISH) experiments confirmed that pri-miR-9-6 is highly expressed in the adult telencephalon whereas pri-miR-9-2 is not detectable (Figures 1B and S1C). Notably, pri-miR-9-6 expression appeared restricted to the first cellular row lining the brain ventricle, composed of the radial glia (RG) that constitute the population of NSCs in this region of the brain (Figure 1B).

To define the expression of miR-9 at a cellular resolution, we performed fluorescent ISH experiments using an antisense LNA probe specific for the mature miR-9 form in combination with astroglial NSCs markers. In the zebrafish pallium, all RG NSCs can faithfully be labeled by immunohistochemistry against GFP in the *gfap:gfp* transgenic line or against glutamine synthase (GS) (Figures S1A and S1B) (Chapouton et al., 2010; Alunni et al., 2013). In contrast to mammals, astrocytes and ependymal cells are absent from the zebrafish pallium, and the only cells that express these markers are RG NSCs (Than-Trong and Bally-Cuif, 2015). In line with the expression of pri-miR-9-6, we could detect mature miR-9 exclusively in RG NSCs (Figure 1C). To confirm the specificity of the signal, we performed additional ISH using two control LNA probes (a scrambled control probe and a probe antisense to miR-9-3p) and two alternative LNA-modified 2′-O-Me RNA oligo probes (Søe et al., 2011) (one control and one miR-9-specific probe). Altogether, these controls demonstrate both the specificity of our miR-9 probe and the stringency of our ISH protocol (Figures S1D and S1E) (LNA probes and their sequences are listed in Table S2).

We next assessed the cycling status of miR-9-expressing NSCs using cycling cell markers such as MCM5, MCM2, or proliferating cell nuclear antigen (PCNA) that can be used interchangeably (Figures S1A and S1B) (Alunni et al., 2013; Chapouton et al., 2006; März et al., 2010). Notably, miR-9-expressing NSCs are almost always quiescent NSCs (qNSCs) (95% ± 2%) (Figure 1C, red arrows), and we could validate a statistically significant association between miR-9 expression and the quiescent state (χ^2 p value < 0.01) (Figures 1C and 1D). In addition, and in contrast to all other NSC markers known to date, miR-9 was found to be expressed only in 47% ± 2% of the overall qNSCs, highlighting a striking heterogeneity in this quiescent population (Figure 1E).

miR-9 expression in a subpopulation of qNSCs could define a distinct NSC sub-lineage, or rather a sub-state in the quiescence cycle of all NSC. To investigate these hypotheses, we interrogated the dynamics of miR-9 expression in NSC in link with their activation history. We applied a short pulse (2 hr) of the thymidine analog bromodeoxyuridine (BrdU), which incorporates into the DNA of dividing cells during S-phase, followed by chase periods of increasing lengths from 1 to 30 days. We then analyzed the expression of miR-9 among $BrdU^+$ NSCs (Figures 1F–1H). After 1 day of chase, no miR-9 was detected in the $BrdU^+$ NSCs (Figure 1H), consistent with the very rare presence of miR-9 expression in dividing glia (Figure 1D). After longer chase periods, miR-9 and BrdU double positive NSCs start to be apparent (Figure 1G, yellow arrow, 1 hr), establishing that miR-9 can be expressed in cells that had previously been actively cycling. The percentage of $BrdU^+$ NSCs expressing miR-9 gradually increased with chase time, suggesting an asynchronous but progressive induction of

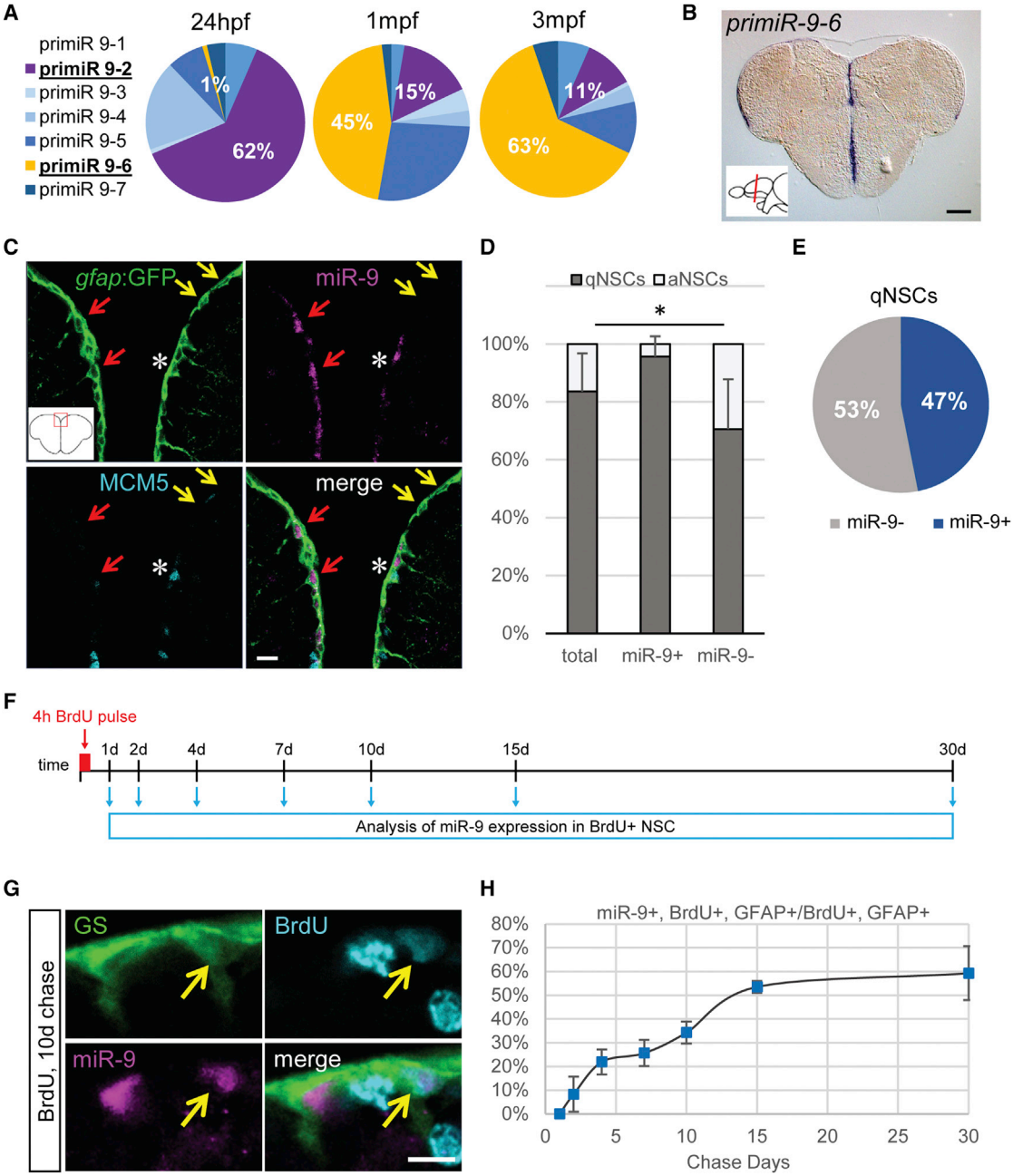

Figure 1. Dynamic Expression of miR-9 in qNSCs

(A) qRT-PCR analysis of the seven miR-9 transcripts in 48 hr post-fertilization (hpf) embryos, 1 month post-fertilization (mpf) juvenile brains, and 3 mpf adult brains with the expression of each transcript over the sum expression of all transcripts.

(B) ISH against pri-miR-9-6 on a cross-section of the telencephalon illustrating its expression restricted to the ventricular region (blue). Scale bar, 100 μm.

(C) Sections through the medial region of the dorsal telencephalon showing ISH with a mature miR-9 LNA probe (magenta) and double fluorescent immunostaining for *gfap*:GFP (green) and MCM5 (light blue). miR-9 expression is restricted to qNSCs (*gfap*$^+$, MCM5$^-$; red arrows) and never observed in aNSCs (*gfap*$^+$, MCM5$^+$; white asterisk). Some qNSCs are devoid of miR-9 signal (yellow arrows). Scale bar, 10 μm.

(D) Proportion of qNSCs (*gfap*$^+$, MCM5$^-$; dark gray) and aNSCs (*gfap*$^+$, MCM5$^-$; light gray) in the total, miR-9$^+$ or miR-9$^-$ NSC population demonstrating that miR-9 expression is associated with quiescence.

(E) Percentage of qNSCs that are miR-9$^+$ or miR-9$^-$.

(F) Experimental design to assess miR-9 expression dynamics across the NSCs activation/quiescence cycle.

(G) Representative image of BrdU$^+$ (light blue), miR-9$^+$ (pink), and GS$^+$ (green) NSC 10 days after BrdU pulse. Scale bar, 5 μm.

(H) Percentage of miR-9$^+$ cells among BrdU$^+$ NSCs after different chase period. *$p < 0.05$; one-way ANOVA with Bonferroni post hoc correction. Data are represented as mean ± 95% confidence interval (CI); n = 3 brains per condition.

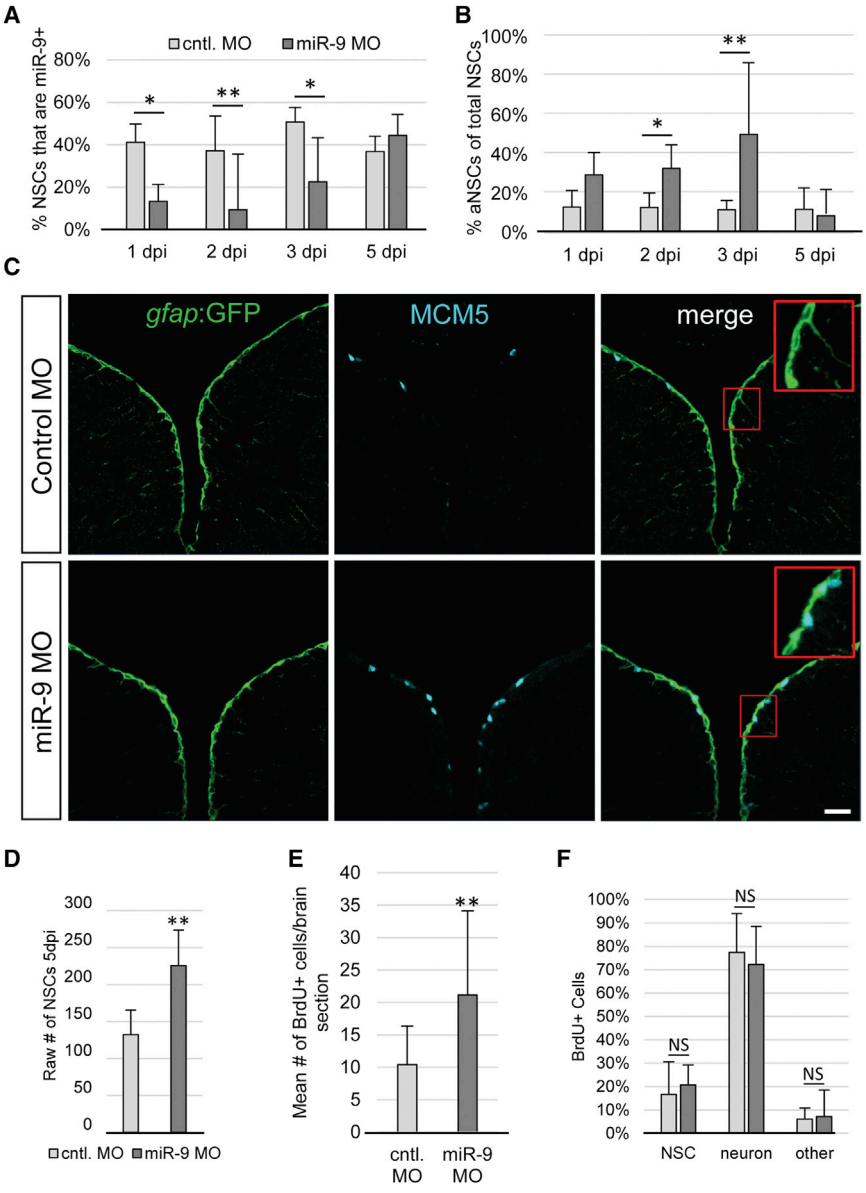

Figure 2. miR-9 Maintains NSC Quiescence

(A) Percentage of NSCs expressing miR-9 at 1, 2, 3, and 5 days post injection (dpi) of the control vivoMO (light gray bars) or miR-9 vivoMO (dark gray bars).

(B) Percentage of aNSCs (MCM5$^+$, *gfap*) over the total NSCs population (*gfap*$^+$) 1, 2, 3, and 5 dpi of the control vivoMO (light gray bars) or miR-9 vivoMO (dark gray bars).

(C) Double immunostaining for *gfap*:GFP (green) and MCM5 (light blue) in control (top) and miR-9 (bottom) vivoMO-injected brains. Scale bar, 20 μm.

(D) Average raw number of *gfap*$^+$ NSCs per section in control (light gray bar) and miR-9 (dark gray bar) vivoMO-treated brains at 5 dpi.

(E and F) Analysis of the fate of activated cells upon miR-9 kd. Fish were administered BrdU for 48 hr following injection of vivoMOs and analyzed after 30 days of chase. (E) Mean number of BrdU$^+$ per brain section in control (light gray bar) and miR-9 (dark gray bar) vivoMO-treated brains. (F) Percentage of BrdU$^+$ cells that remain NSCs (*gfap*$^+$), or acquired a neuronal fate (HuC/D$^+$) or other fate in control (light gray bar) and miR-9 (dark gray bar) vivoMO and brains after a 30 day chase. *$p < 0.05$, **$p < 0.01$; one-way ANOVA with Bonferroni post hoc correction. Data are represented as mean ± 95% CI; n = 3 brains per condition.

miR-9 expression among NSCs after cell division, to reach a plateau at ~50% (Figure 1H), matching the overall proportion of qNSCs that express miR-9 (Figure 1E). Knowing that most pallial NSCs are capable of dividing (Alunni et al., 2013), these data together reveal that expression of miR-9 highlights a specific sub-state of quiescence in which qNSCs dynamically progress through.

miR-9 Maintains Quiescence

Does miR-9 actually play some role in controlling NSC quiescence? To address this issue, we performed loss-of-function experiments. Vivo morpholino oligonucleotides (vivoMO) are covalently linked to a delivery moiety conferring them the ability to enter into a cell without the need for transfection. Injection of a vivoMO into the brain ventricle enables the modulation of gene expression in the first ventricular cell rows, most notably in the RG NSC layer (Kizil and Brand, 2011). We used a miR-9 antisense vivoMO that binds to the mature miR-9 rendering it essentially inactive. The sequence of this vivoMO is identical to the MO previously validated to efficiently inhibit miR-9 in zebrafish embryos, without showing any evidence for off-targets effects (Kloosterman et al., 2007; Leucht et al., 2008) (Table S1). By performing an ISH with the mature miR-9 antisense probe, we verified that the miR-9 vivoMO also efficiently and specifically blocks miR-9 in the adult pallium, for up to 3 days post injection (dpi) (Figures 2A and S2A). To determine the effect of miR-9 knockdown (kd) we analyzed the ratios of NSC activation status by quantifying GFAP$^+$/MCM5$^-$ (qNSC) and GFAP$^+$/MCM5$^+$ (aNSC) in control vivoMO- and miR-9 vivoMO-treated brains. In conditions of miR-9 kd, we observed, on average, a 3-fold increase in the proportion of aNSCs that was maintained for as long as the vivoMO was active (Figures 2B and 2C). After 3 days of miR-9 kd, this increase in aNSCs parallels the proportion of qNSCs that endogenously express miR-9 demonstrating that almost all of the miR-9 expressing NSCs enter into the cycle thus establishing miR-9 as a potent regulator of quiescence. To confirm the specificity of the miR-9 vivoMO effect, we used a combination of vivoMOs designed to target Drosha-processing sites on pre-miR-9 sequences (processing MO1, MO6), thereby blocking

miR-9 production (Figure S2B; Table S1). Upon injection, these morpholinos efficiently reduce mature miR-9 levels, both in embryos and in the adult pallium (Figures S2C and S2D). Consequently, and consistent with the effect of the vivoMO targeted against mature miR-9, a significant increase in the proportion of aNSCs is observed, confirming the specific effect of miR-9 kd on NSCs activation (Figure S2E). We also verified that injections of vivoMOs do not induce any apoptosis or inflammatory reaction, a process known to activate NSCs in the zebrafish pallium (Figure S2F) (Kizil et al., 2012; Kyritsis et al., 2012), nor any induction of *gata3* expression (Figure S2F), previously shown to mediate NSCs activation upon inflammation or lesion (Kizil et al., 2012; Kyritsis et al., 2012). The increase in aNSCs observed upon miR-9 kd is thus not related to a regenerative response but rather a consequence of an imbalance in constitutive neurogenesis regulation.

Interestingly, at 5 dpi, the vivoMO appears to be no longer active in blocking miR-9 (Figures 2A and S2A) and the proliferation rate of NSCs returns to basal levels (Figure 2B). Nevertheless, the NSCs activated upon miR-9 blockade proceed through mitosis, as demonstrated by an increase in the total number of RG NSCs lining the VZ at 5 dpi (Figure 2D), which is also in agreement with most NSC divisions being symmetric in the short term (Rothenaigner et al., 2011). To better appreciate the long-term effect of miR-9 blockade on neurogenesis, we administered BrdU for 48 hr after vivoMO injections and analyzed the fate of dividing cells 30 days later by immunohistochemistry against NSC and neuronal markers (GS and Hu, respectively). The raw number of $BrdU^+$ cells per section was doubled in the miR-9 vivoMO condition as compared to controls (Figure 2E), which is consistent with the transient increase in proliferation we observed in the short term. However, there was no significant difference in the relative proportions of the different cell types generated between the two conditions (Figure 2F). This shows that upon miR-9 blockade, NSCs only increase their propensity to enter the cell cycle, while their fate potential and clonal behavior appear unchanged. Overall, these data reveal that the primary role of miR-9 is maintaining quiescence of NSCs.

miR-9 Potentiates Notch Signaling to Promote Quiescence

Zebrafish pallial NSC quiescence is maintained through active Notch signaling (Chapouton et al., 2010; Alunni et al., 2013). To investigate the relationship between miR-9 and Notch, we first analyzed the effect of Notch blockade on miR-9 expression: fish were treated for 48 hr with LY411575 (LY), a potent derivative of the γ-secretase inhibitor DAPT, which efficiently blocks Notch signaling and consequently pushes qNSCs into cell cycle re-entry (Figures S3A and S3B) (Alunni et al., 2013). qRT-PCR experiments revealed that the levels of the seven pri-miR-9 transcripts were not affected by Notch inhibition, in contrast to the direct Notch target gene *her4* (Figure 3A). Additionally, Notch inhibition had no effect on mature miR-9 levels (Figure 3B), establishing that miR-9 expression is not regulated by Notch in adult NSCs. These results were surprising as inhibiting Notch using LY leads to a significant increase in aNSCs and miR-9 is normally never endogenously expressed in these cells (Figure 1D). To investigate this discrepancy, we analyzed the expression of miR-9 in NSCs by ISH upon Notch blockade. In contrast to the control situation, we could observe miR-9 expression in $PCNA^+$ cells that were activated upon Notch blockade (Figure 3C, yellow arrow). In fact, upon LY treatment, a similar proportion of activated cells is observed among miR-9^+ or miR-9^- NSCs, and there is a loss of the preferential association of miR-9 with the quiescent state (DMSO: χ^2 p value < 0.05; LY: χ^2 p value = 0.87) (Figure 3D). Downregulation of miR-9 is thus not an absolute requirement for cell-cycle entry, at least in this context. Moreover, these data demonstrate that when Notch signaling is impaired, miR-9 is no longer able to inhibit cell-cycle entry thus suggesting that miR-9 could act upstream of Notch in quiescence regulation. In line with this idea, we observed that the expression of the Notch effector *her4* is downregulated upon miR-9 kd (Figure 3E), as well as the expression of another known Notch target gene encoding the Notch-regulated ankyrin repeat protein (*nrarpa*) (Figures S3D and S3E). By contrast, we do not observe a concomitant decrease in the expression of the *notch3* receptor gene, the main *notch* receptor gene expressed in qNSCs (Alunni et al., 2013) (Figure S3C). To further challenge our hypothesis, we performed epistasis experiments in which we assessed the effect of miR-9 kd in NSCs with constitutively activate Notch signaling. Ventricular NSCs were electroporated with an expression construct encoding a Myc-tagged Notch intracellular domain (NICD) (Takke et al., 1999), followed by injection of the miR-9 vivoMO. We observed that overexpression of NICD locks NSCs in a quiescent state, as expected, and also erases the activating effect of miR-9 depletion (Figure 3F). Altogether, our results suggest that miR-9 maintains NSC quiescence by potentiating Notch activation (Figure S3F).

miR-9 Is Concentrated in the Nucleus of Mature RG NSCs and Is Strongly Associated with Nuclear Localization of Ago Proteins

When analyzing the expression of miR-9 in the adult pallial NSCs, we made the surprising observation that mature miR-9 molecules were strongly concentrated in the nuclei of qNSCs (Figure 4A, yellow arrow) (as stated previously, miR-9 is not detectable in aNSCs) (Figure 4A, red arrow). This result was unexpected, as canonically, mature microRNAs influence gene expression via post-transcriptional regulation of mRNA in the cytoplasm (Bartel, 2009). Importantly, we observed no nuclear concentration of miR-9-3p in ventricular NSCs (Figure S1D) thus arguing against a nuclear trapping of unprocessed pri-miRs. In addition, we assessed the expression of another neurogenic microRNA, let-7b, whose expression pattern in the zebrafish embryo closely resembles that of miR-9 (Wienholds et al., 2005). In the adult pallium, we found let-7b expression to be localized to the first ventricular rows, encompassing RG cells and differentiating neuronal precursors (Figure S4A); however, in contrast to miR-9, let-7b localizes almost exclusively to the cytoplasm (Figure S4A′). The localization of miR-9 in adult NSC nuclei is also in complete contrast to the exclusively cytoplasmic localization of miR-9 in embryonic or juvenile pallial neural progenitors (NPCs) (Figure 4B). The specific nuclear enrichment of mature miR-9 in adult NSCs compared to juvenile NSCs was also confirmed by qRT-PCR on cytoplasmic and nuclear

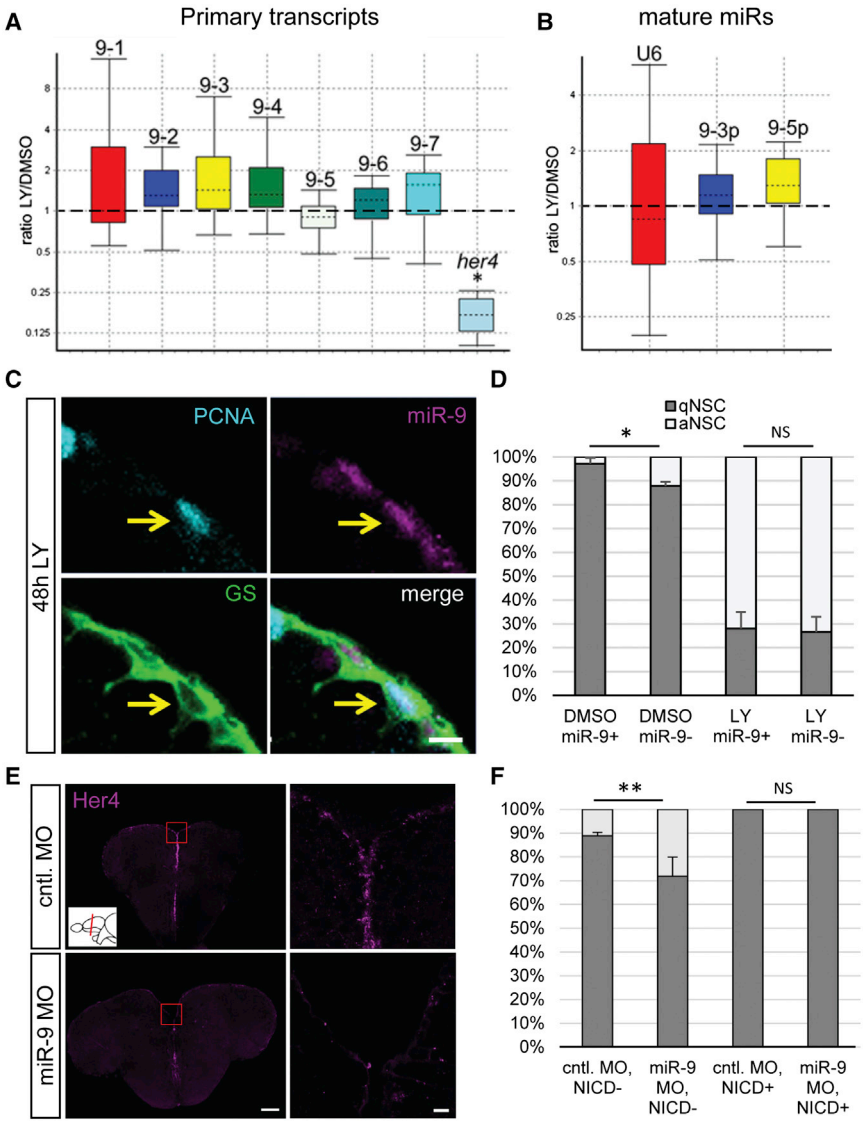

Figure 3. miR-9 Potentiates Notch Activity to Maintain Quiescence

(A and B) Boxplots of qRT-PCR analysis showing the relative change in expression of the miR-9 transcripts and the Notch target *her4* (A) and of the mature miR-9-5p/3p compared to a U6 small nucleolar RNA (snoRNA) control (B) after a 48 hr treatment with LY411575 or DMSO (control). The top and the bottom of each box indicate the 75th and 25th percentiles, respectively, and the dotted line indicates the median.

(C) Expression of miR-9 (magenta) in a GS^{+} (green)/PCNA^{+} (light blue) aNSC (yellow arrow) after a 48 hr LY treatment. Scale bar, 5 μm.

(D) Proportion of qNSCs (*gfap*$^{+}$, MCM5^{-}; dark gray) and aNSCs (*gfap*$^{+}$, MCM5^{+}; white) in the miR-9^{+} or miR-9^{-} NSC population after a 48 hr treatment with LY or DMSO.

(E) ISH for *her4* 2 dpi with the control (top) or miR-9 (bottom) vivoMO. Right panels are close-ups of the region within the red box. Scale bars, 100 μm (left); 50 μm (right).

(F) Epistasis experiment combining miR-9 kd with overexpression of Notch intracellular domain (NICD). The graph shows the percentage of qNSCs (dark gray) and aNSCs (white) in brains injected with the control or miR-9 vivoMO and in cells overexpressing NICD (NICD^{+}) or not (NICD^{-}). *$p < 0.05$, **$p < 0.01$; one-way ANOVA with Bonferroni post hoc correction. Data are represented as mean ± 95% CI; n = 3 brains per condition.

fractions (Figure S4B). These data reveal a switch in the subcellular localization of miR-9, from the cytoplasm of NPCs to the nucleus of mature qNSCs, further reinforcing a link between miR-9 and a distinct quiescent state.

To assess the functional relevance of this observation, we reasoned that active miR-9 should be loaded into Argonaute proteins (Ago), the main effectors of the microRNA silencing pathway (Meister, 2013), and therefore analyzed the subcellular localization of Ago proteins in the zebrafish pallium. We utilized two independent Ago antibodies that recognize highly conserved portions spanning the PIWI and most of the MID domains of human Ago2 (Figure S4C). Both detect a band at the expected size in western blot (WB) from adult brain extracts, matching the size of overexpressed zebrafish Flag-Ago2 (Figures S4D and S4E, red arrows). Additionally, when performing immunohistochemistry on adult NSCs electroporated in vivo with a Flag-Ago2 expression construct, we observed overlapping signals for Flag and Ago (Figure S4G). As the C-terminal portion is highly conserved among all vertebrate Agos, however (Figure S4C), we cannot preclude that our antibodies label other Ago proteins than Ago2, and indeed, they have been shown previously to detect other Agos (1, 3, and 4) in human samples (Flores et al., 2014; Nelson et al., 2007); we thus refer to "Ago" staining below. Strikingly, we observed that Agos are highly expressed in the nuclei of a subset of NSCs (Figure 4D, yellow arrows) while in other NSCs the expression of Agos is either exclusively cytoplasmic (Figure 4D, white asterisk) or diffuse throughout the cell (Figure 4D, gray arrow). Importantly, the presence of Agos in cell nuclei was validated using both Ago antibodies (Figure S4F) and confirmed by subcellular fractionation of proteins from telencephalic extracts (Figure S5D). We also observed a nuclear enrichment of Agos in neurons located in the deep brain parenchyma, strikingly associated with the nuclear localization of neuronal microRNAs such as miR-128 (Figures S5A and S5B). Notably, the presence of Agos in nuclei was restricted to adult stages, as Agos are exclusively located in the cytoplasm of juvenile NPCs and neurons (Figure S5C).

Focusing on NSCs, we could show that, like miR-9, nuclear Ago staining is significantly associated with quiescence and we rarely see Agos in the nucleus of aNSCs (Figures S5E and

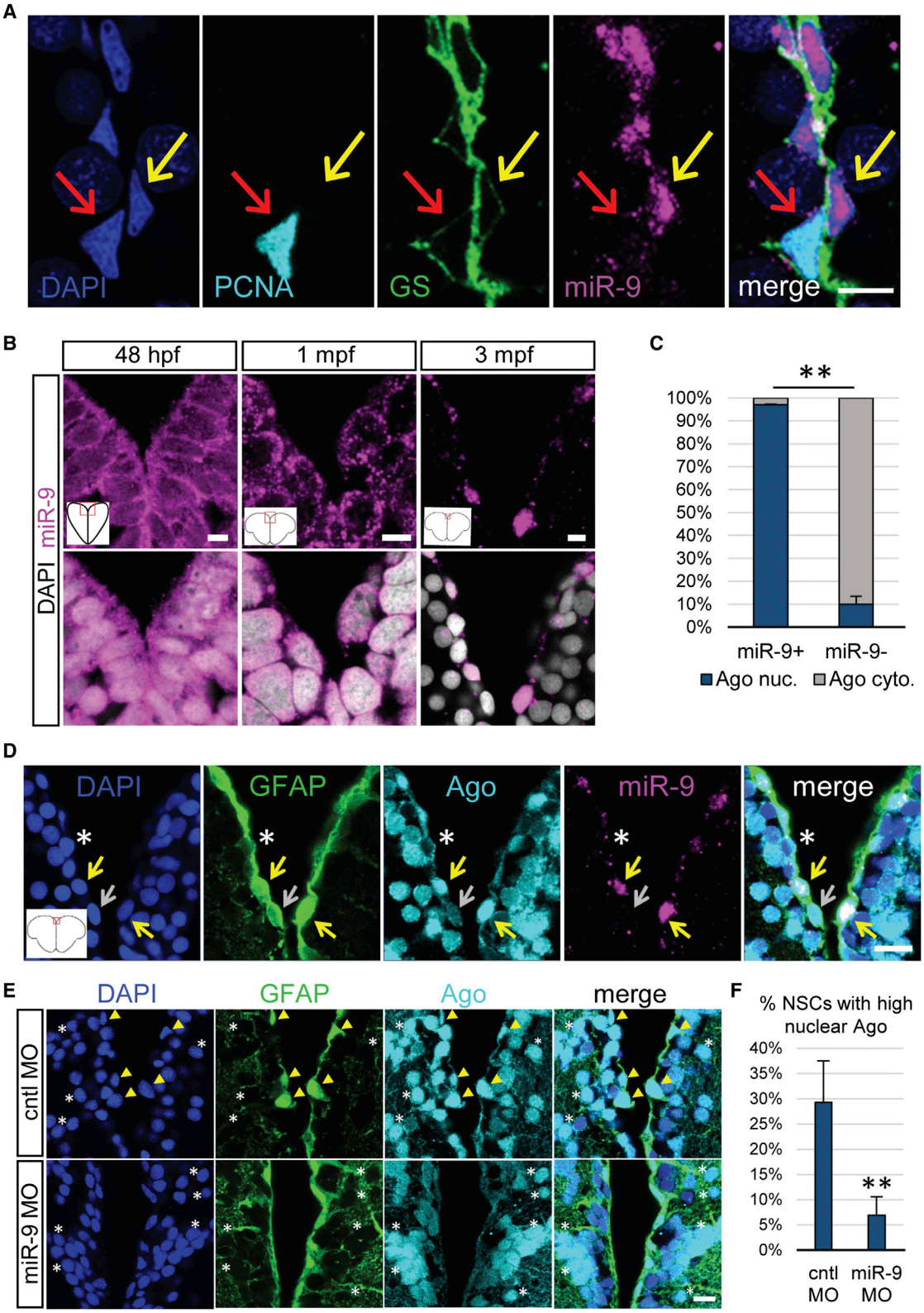

(legend on next page)

S5F). Importantly, we also observed a strong association between the localization of Agos and miR-9 (χ^2 p value < 0.01) (Figure 4C): in miR-9-expressing qNSCs Agos are mostly found in the nucleus (Figure 4D, yellow arrows), while in miR-9-negative NSCs Agos are mostly cytoplasmic (Figure 4D, white asterisk and gray arrow). Lastly, and remarkably, when we knock down miR-9 we find a significant reduction in the proportion of NSCs displaying high levels of Agos in the nucleus (control MO = 29% ± 8%; miR-9 MO = 7% ± 4%) (Figures 4E and 4F). By contrast, we still observe a nuclear localization of Agos in neuronal cells of the parenchyma, demonstrating that this effect is specific to ventricular cells (Figure 4E, asterisks). This further strengthens the correlation between nuclear miR-9 and nuclear Agos; yet, based on these data, we cannot rule out the possibility that the change of Ago localization upon miR-9 kd is an indirect result of the increase in aNSCs number, which never have nuclear Agos.

Ago Proteins Actively Shuttle between the Cytoplasm and Nucleus that Impacts miR-9 Localization

To test the biological relevance of nuclear Agos in link with the control of NSC quiescence, we first examined whether active nuclear/cytoplasmic shuttling of Agos occurs in vivo in qNSCs. Recently, an essential protein component of the RISC, TNRC6A (GW182), was shown to shuttle Ago2 between the cytoplasm and the nucleus in human HeLa cells, while being re-cycled out of the nucleus in an Exportin 1-dependent manner (Nishi et al., 2013). We cloned a region spanning two of the GW regions of the zebrafish *tnrc6a* gene (Figure 5A) and fused it with a GFP tag. These two GW domains were previously demonstrated to mediate binding of TNRC6A to Ago proteins in mammals (Eulalio et al., 2008). We confirmed by co-immunoprecipitation experiments in zebrafish embryos that the GFP-fused protein fragment binds both overexpressed FLAG-tagged Ago2 and endogenous zebrafish Ago proteins (Figure S6A). Moreover, overexpression of this construct in embryos dose-dependently interferes with miRNA silencing as shown in sensor assays (Figure S6B). Importantly, the TNRC6 fragment lacks a nuclear localization signal, hence is unable to enter into the nucleus thus acting as a dominant-negative TNRC6 (DN-TNRC6) cytoplasmic Ago-trap. To preferentially target qNSCs, we placed this construct under the promoter of the Notch-target gene *her4* (*her4:dn-tnrc6-gfp*) and electroporated it into the VZ of the adult pallium. In contrast to GFP, the DN-TNRC6-GFP fusion protein localizes mostly cytoplasmically (Figure 5B, white arrow). Strikingly, Agos were rarely nuclear in the NSCs that received *her4:dn-tnrc6-gfp* (12% ± 8%; Figure 5B, white arrow), as opposed to NSCs electroporated with the control *her4:gfp* (64% ± 5%; Figure 5B, yellow arrow) thus confirming cytoplasmic trapping of Agos (Figures 5B and 5C). Additionally, miR-9 expression is completely absent from the nuclei of the RG electroporated with *her4:dn-tnrc6-gfp* (Figures 5D and S6C). Next, in a reciprocal experiment, we inhibited Exportin 1 by injecting Leptomycin B (LMB) into the brain ventricle. This treatment led to a significant increase in NSCs displaying a strong nuclear Ago signal (Figure 5E, yellow arrowheads; quantified in Figure 5F) thus establishing that Agos can be transported to and maintained in the nucleus. LMB administration concomitantly increased the number of cells displaying a strong nuclear signal for miR-9 (Figures S6D and S6E). In sum, we were able to demonstrate that an active shuttling of Agos does indeed occur in vivo in NSCs, and specifically, their nuclear export is dependent on Exportin-1 and their nuclear import requires an interaction with TNRC6. Moreover, our data also indicate that the presence of miR-9 in the nucleus is reliant on nuclear Agos.

The Nuclear Localization of miR-9/Agos Is Necessary for NSC Quiescence

Next, we wanted to evaluate whether manipulating the ratio of nuclear to cytoplasmic Agos in NSCs impacts cell state. To do this, we assessed the levels of NSC activation in the LMB-treated and *her4:dn-tnrc6-gfp*-electroporated brains. In the context of LMB-treated brains, the increased nuclear concentration of Agos and miR-9 was correlated with a significant increase in NSC quiescence (Figures 5E and 5G). In epistasis experiments, this increase in quiescence was rescued by injection of miR-9 vivoMO, thus establishing a causal link between maintaining miR-9/Agos complexes in the nucleus and the quiescent state (Figure 5H). By contrast, we found that NSCs overexpressing DN-TNRC6 were 2.5-fold more likely to enter into the cell cycle when compared with control NSCs expressing GFP (Figures 5B and 5I). Notably, the fold increase in NSC activation that was reached upon expressing DN-TNRC6 matches the one observed in conditions of miR-9 kd (Figure 2B). Moreover, knocking down miR-9 in conditions in which Ago/miR-9 complexes are excluded from the nucleus, via application of the

Figure 4. miR-9 Is Nuclear in Mature qNSCs and Is Significantly Associated with the Nuclear Localization of the RISC Effector Ago

(A) Representative image of ISH for miR-9 (magenta) and double immunostaining for PCNA (light blue) and GS (green) with nuclear DAPI counterstaining (dark blue) highlighting the presence of miR-9 in the nucleus of qNSCs (yellow arrow) and not in the nucleus of aNSCs (red arrow). Scale bar, 10 μm.

(B) Sections through the medial region of the dorsal telencephalic ventricle of a 48 hpf embryo, a 1 mpf juvenile, and a 3 mpf adult zebrafish illustrating an ISH of miR-9 (magenta) alone (top) and together with DAPI counterstaining in gray (bottom). Scale bar, 5 μm.

(C) Proportion of cells showing strong nuclear localization of Ago (blue) or mostly cytoplasmic localization of Ago (light gray) in miR-9$^+$ versus miR-9$^-$ NSCs populations, illustrating the association between nuclear Ago localization and miR-9 expression.

(D) ISH of miR-9 (magenta) and double fluorescent immunostaining for *gfap*:GFP (green) and Ago (ab57113, light blue) with nuclear DAPI counterstaining (dark blue). Strong nuclear Ago localization is observed in miR-9$^+$ NSCs (yellow arrows) in contrast to cytoplasmic Ago localization in miR-9$^-$ NSCs (white asterisk and gray arrow). Scale bar, 20 μm.

(E) Double fluorescent immunostaining for *gfap*:GFP (green) and Ago (light blue) with nuclear DAPI counterstaining (dark blue) in conditions of miR-9 kd (bottom) when compared to controls (top). NSCs with strong nuclear Ago staining (yellow arrowheads) are lost in miR-9 MO-treated brains, while the nuclear signal for Ago in neuronal cells is not affected by miR-9 kd (white asterisks). Scale bar, 10 μm.

(F) Quantification of the percentage of NSCs displaying a strong nuclear Ago signal 2 dpi of the control or miR-9 vivoMO. **p < 0.01; one-way ANOVA with Bonferroni post hoc correction. Data are represented as mean ± 95% CI; n = 3 brains per condition.

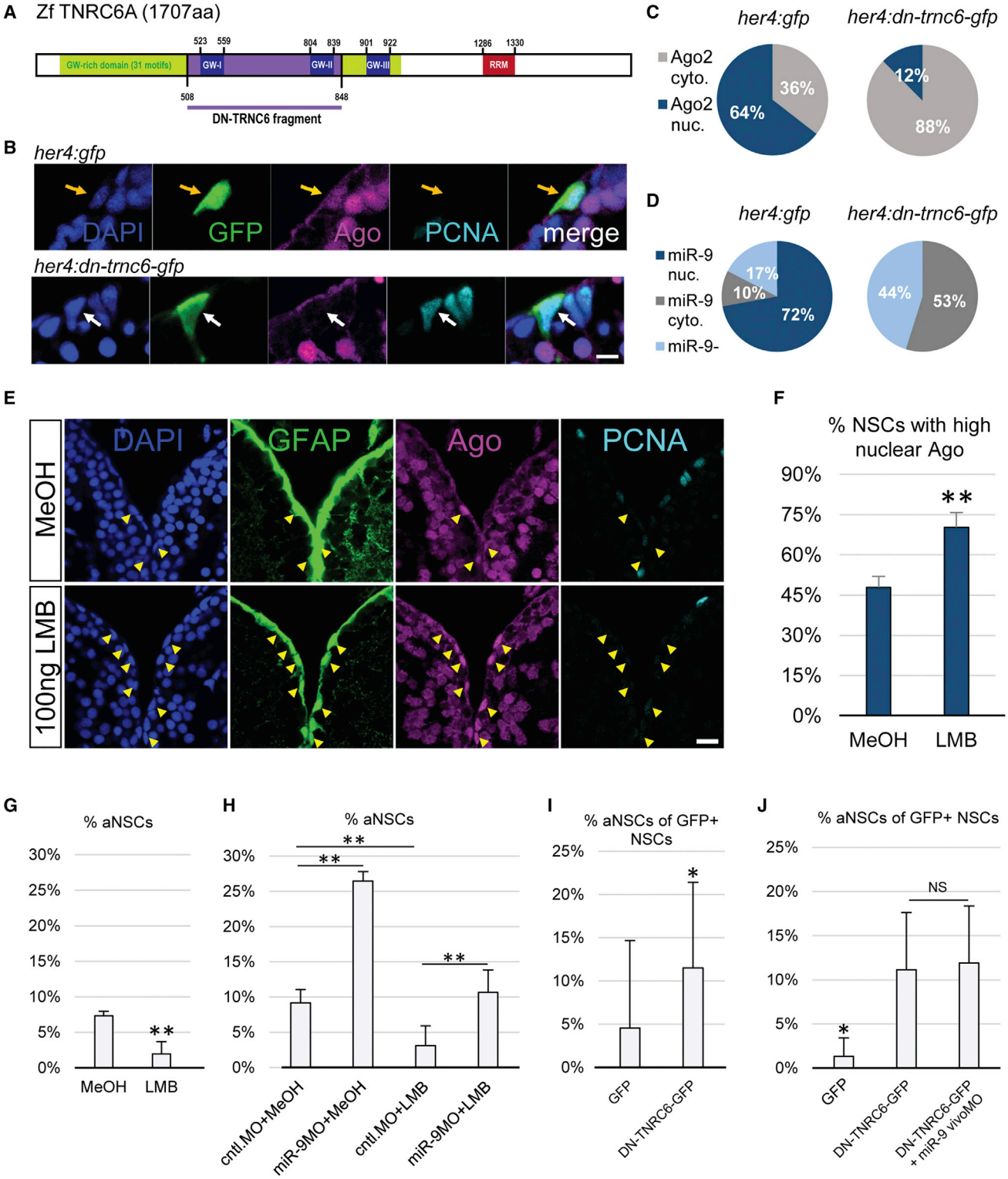

Figure 5. Active Nucleo-Cytoplasmic Shuttling of Ago and miR-9 Impacts the Quiescent State of NSCs

(A) Scheme of the zebrafish TNRC6 protein with the cloned GW-rich Ago binding domain highlighted in purple.

(B) Triple immunofluorescence of GFP (green), Ago (magenta), and PCNA (light blue) with nuclear DAPI counterstaining (dark blue) on a representative cell electroporated with a control construct (*her4:gfp*, top, yellow arrow) or the dominant-negative TNRC6 (DN-TNRC6) construct (*her4:dn-tnrc6a-gfp*, bottom, white arrow). Scale bar, 5 μm.

(legend continued on next page)

miR-9 vivoMO after electroporation of DN-TNRC6, does not show an additive effect on proliferation (Figure 5J). This second epistasis experiment further indicates that nuclear miR-9 is indeed the active miR-9 pool in NSC quiescence control. Altogether, these data suggest that Agos and miR-9 require each other to be actively and concomitantly shuttled from the nucleus to the cytoplasm in a TNRC6-dependent manner, and their subcellular localization impacts cell state. In addition, their presence in the nucleus is coupled with increased levels of quiescence.

Nuclear miR-9 and Ago Localization Are Conserved in Quiescent NSCs of the Adult Mouse Brain

Adult NSCs in the zebrafish and mammalian pallium share molecular and cellular similarities, including their dependence on Notch signaling for quiescence (Than-Trong and Bally-Cuif, 2015), suggesting that the miR-9/Ago process discovered above may also be shared. To address this, we examined whether the nuclear localization of miR-9 and Agos is conserved and linked with quiescence control in adult mouse NSCs. At a global level, ISH experiments revealed the expression of miR-9 to be high in the SEZ and DG, the two known areas of constitutive neurogenesis in the adult mammalian brain (Figure S7A). No signal was obtained using a control scrambled probe, demonstrating the specificity of our staining (Figure S7B). We then analyzed the expression of miR-9 in conjunction with GFAP and Sox2, a SRY-related HMG box family member transcription factor demonstrated to be expressed in NSCs (quiescent and activated) of the DG and SEZ (Hsieh, 2012; Suh et al., 2007). Strikingly, we observe miR-9 in the nucleus of a subset of NSCs in both regions (Figures 6A and 6B, yellow arrows). In contrast to what we observed in zebrafish, miR-9 appears to be additionally expressed in other cell types, although with a cytoplasmic localization. Very infrequently $Sox2^+$ NSCs are found to be actively proliferating and express Ki67, however, like in zebrafish, we did not detect miR-9 in the nucleus of these aNSCs (Figure S7C). We also compared the proportion of $GFAP^+$ $Sox2^+$ NSCs that express miR-9 in the nucleus between young (2-month-old) and older (10-month-old) mice in the DG. Interestingly, we observed a significant increase in miR-9 nuclear localization, suggesting a maturation-associated shift in the subcellular localization of miR-9 (Figure 6C). Overall, this in vivo data suggest that, like in zebrafish NSCs, nuclear miR-9 is associated with a mature quiescent NSC state in the mouse brain.

In the DG, BMP signaling maintains NSC quiescence and cultured NSCs from mice and rats have been shown to enter into a state of reversible cell-cycle arrest when treated with BMP ligands (Mira et al., 2010; Martynoga et al., 2013). Transcriptomic analysis demonstrated that this cell-cycle arrest is equivalent to endogenous quiescence (Martynoga et al., 2013) thus making these cells an ideal tool in which to probe the subcellular localization of Agos and miR-9 upon synchronous quiescence entry. For our analysis, we utilized in vitro NSCs isolated from the DG of adult mice (AH-NSCs). When cultured in the presence of the mitogen epidermal growth factor (EGF), these AH-NSCs are actively proliferating as demonstrated by the expression of the cell-cycle marker MCM2 (Figure S7D). These cells, when cultured for 3 days without EGF and in the presence of BMP4, downregulate MCM2 and upregulate GFAP expression (Figures S7D and S7E). We could observe that proliferating NSCs tend to display low levels of Agos and miR-9 inside their nuclei, while quiescent AH-NSCs display a dramatic increase in the nuclear concentration of Ago2 and miR-9 (Figure 6D). Quantitative analysis shows that up to 60% of AH-NSCs harbor strong nuclear signals for Agos and miR-9 when they are induced to quiescence by BMP4 (Figures 6E and 6F). The increase in nuclear localization of these two factors was confirmed by automated quantification of relative signal intensities in cytoplasmic and nuclear compartments (Figure 6G). By contrast, we did not detect any significant change in total levels of Ago2 protein (Figure S7F). Altogether, these in vivo and in vitro data point to a conserved association between nuclear Agos and miR-9 with quiescence in murine NSCs.

DISCUSSION

Our study identifies a microRNA, miR-9, as a critical player in the regulation of zebrafish pallial NSCs quiescence, a defining and protective feature of adult tissue stem cells (Cheung and Rando, 2013). Other microRNAs have been shown to be pivotal in regulating the proliferative behavior of adult tissue stem cells, such as in the muscle (Cheung et al., 2012; Crist et al., 2012; Sato et al., 2014) or skin (Wang et al., 2013). Interestingly, in our case, we also observed that miR-9 is expressed in only half of the qNSCs. Further, BrdU pulse-chase experiments demonstrated that, after cell division, there is a short refractory period after which miR-9 expression is progressively induced in NSCs. The proportion of miR-9-expressing cells in the BrdU label-retaining NSCs never exceeds this of the overall NSCs population, indicating that miR-9 expression highlights a transitory phase qNSCs shuttle through. Our data thus highlight the importance of division history and temporal competence for the establishment of miR-9 expression in qNSCs and identify miR-9 as a molecular marker

(C) Quantification of the data from (B), showing the percentage of electroporated cells with mostly nuclear (blue) or cytoplasmic (gray) Ago signal; n = 10 brains per condition.
(D) Percentage of cells electroporated with the *her4:gfp* (top) or *her4:dn-tnrc6-gfp construct* (bottom) in which miR-9 is detected in the nucleus (dark blue), cytoplasm (gray) or absent (light blue); n = 10 brains per condition.
(E) Triple fluorescent immunostaining of *gfap*:GFP (green), Ago (magenta), and PCNA (light blue) with nuclear DAPI counterstaining (dark blue) after ventricular injection of LMB (bottom) or a MeOH control (top). Yellow arrowheads highlight NSCs with a strong nuclear Ago signal. Scale bar, 20 μm.
(F and G) Quantification of data from (E) 24 hpi with LMB or MeOH as a control; n = 5 brains per condition. (F) Percentage of NSCs ($gfap^+$) with strong nuclear Ago signal. (G) Percentage of aNSCs ($PCNA^+$, $gfap^+$) among NSCs ($gfap^+$).
(H) Percentage of aNSCs ($PCNA^+$, $gfap^+$) among NSCs ($gfap^+$) upon combination of LMB or MeOH injections with vivoMO injections. n = 4 brains per condition.
(I) Quantification of the data from (B) of the percentage of GFP^+ aNSCs out of total GFP^+ NSCs; n = 10 brains per condition.
(J) Percentage of aNSCs ($MCM2^+$, GFP^+) out of total NSCs (GFP^+) after electroporation with the control *her4:gfp* or *her4:dn-tnrc6-gfp* construct and subsequent MO injections. n = 7 brains per condition. *$p < 0.05$, **$p < 0.01$; one-way ANOVA with Bonferroni post hoc correction. Data are represented as mean ± 95% CI.

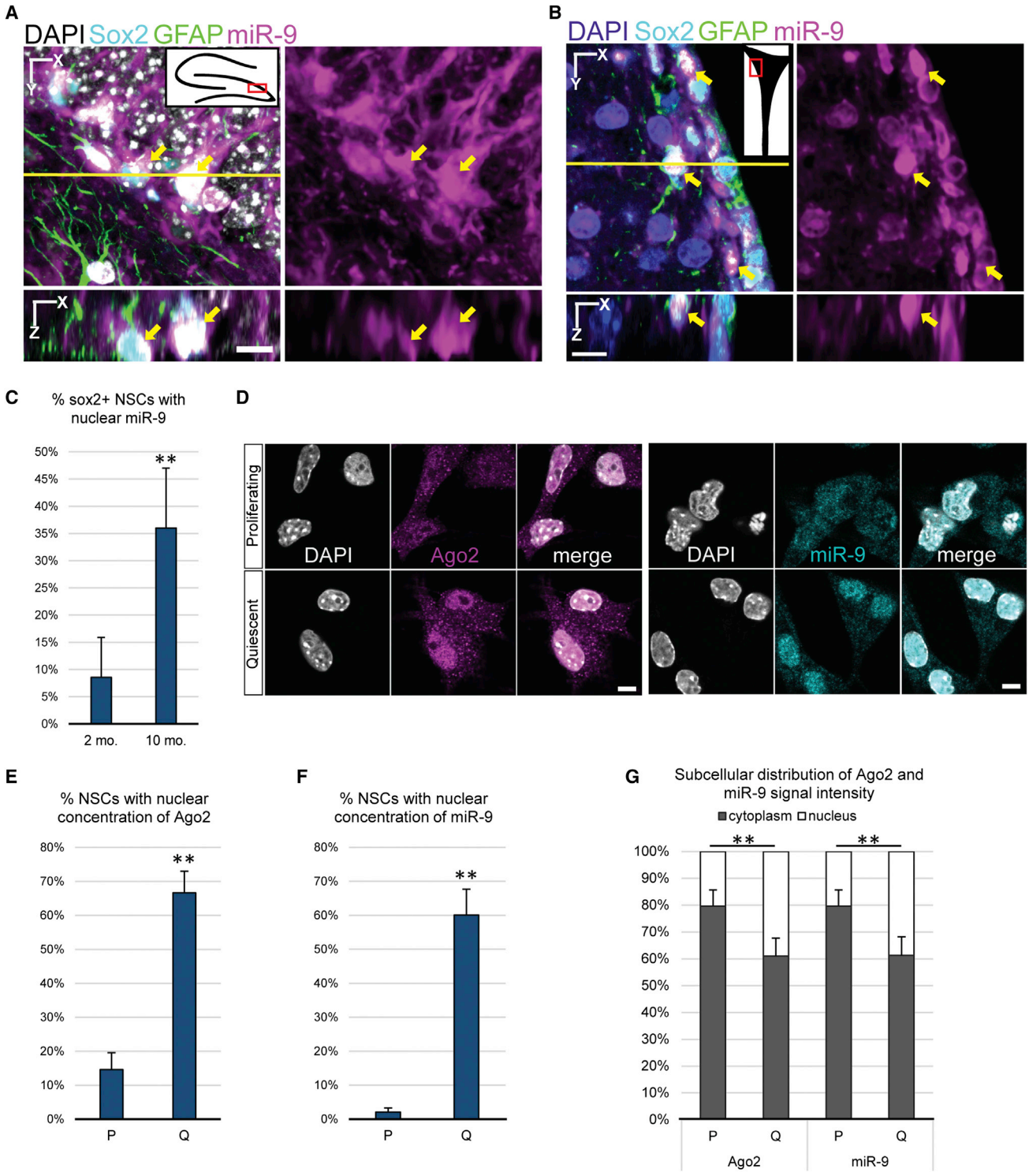

Figure 6. Nuclear Localization of miR-9 and Ago2 Also Correlates with Quiescence in Adult Mouse NSCs

(A and B) Representative high-magnification two-dimensional images of the 10-month DG (A) and SEZ (B) on the XY (top) and YZ (bottom) axes (yellow line = position of the YZ image) with Sox2 (light blue) and GFAP (green) immunofluorescence, miR-9 ISH (magenta), and a nuclear DAPI counterstain (gray). Scale bars, 10 μm.

(C) Percentage of NSCs ($Sox2^+$, $GFAP^+$) with nuclear miR-9 in the DG of 2- and 10-month mouse brains; n = 2 brains per age. *$p < 0.05$; one-way ANOVA with Bonferroni post hoc correction. Data are represented as mean ± 95% CI.

(legend continued on next page)

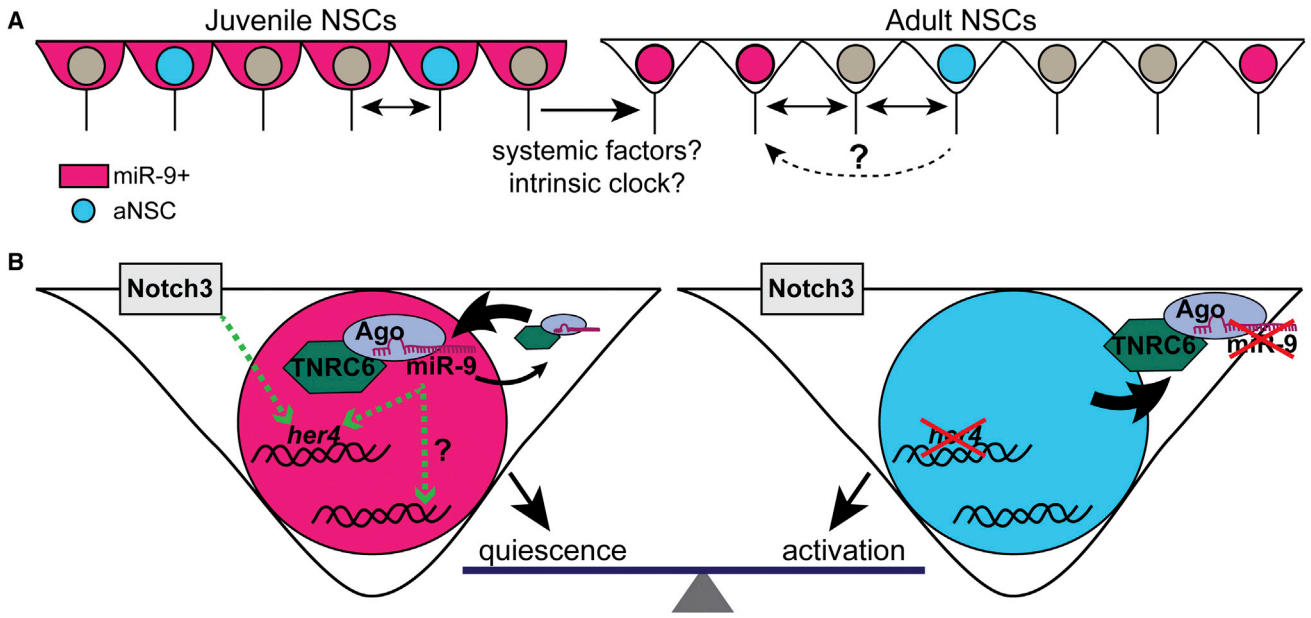

Figure 7. Model for Ago/miR-9 Complexes in Regulating NSCs Quiescence

(A) miR-9 is concentrated in the cytoplasm of all juvenile NSCs (qNSCs and aNSCs). In the adult, miR-9 is concentrated in the nucleus of ~50% of the qNSCs. Adult qNSCs cycle between miR-9^{+} and miR-9^{-} states.

(B) In adult qNSCs (left), Ago (light purple)/miR-9 (magenta) complexes are actively shuttled into the nucleus by TNRC6 proteins (dark green). Enhanced transport of Ago/miR-9 complexes into the nucleus anchors the NSCs in quiescence via directly or indirectly activating *her4* expression in concert with Notch3 and through other unknown mechanisms, perhaps by influencing chromatin state. Upon transport of Ago/miR-9 complexes into the cytoplasm, the NSC is activated (right) and miR-9 is no longer detectable, demonstrating that TNRC6-mediated shuttling of Ago/miR-9 is necessary for balancing the quiescent versus activated NSC state.

of a heterogeneity among qNSCs. Previous studies applying genetic labeling and lineage tracing have demonstrated that NSCs in the adult mouse DG are also heterogeneous in their activation potential and contribution to long-term neurogenesis (Giachino and Taylor, 2014; Lugert et al., 2010). Unveiling the precise properties linked with miR-9 expression, in terms of differential molecular control of activation and fate potential upon division will ultimately help understanding the establishment of heterogeneity within qNSCs and its functional significance for NSCs population dynamics.

Many similarities and differences between the nature and regulation of embryonic NPCs and adult NSCs have been identified (Urbán and Guillemot, 2014), however, the modifications in stem cell properties and molecular control between juvenile and adult stages are still rather understudied. Interestingly, a recent study revealed a progressive change in the expression of cell-cycle regulators in BLBP-positive RG during post-natal stages in mice, directly influencing the competence of these cells to be transformed by oncogenes (Muñoz et al., 2013). Moreover, a change in microRNAs signature occurs in muscle satellite stem cells between juvenile and adult stages and correlates with a modification of cell-cycle dynamics (Sato et al., 2014). Our data provide important molecular insights on this transition. First, we show that the relative expression of the miR-9 primary transcripts changes progressively from the embryo to the adult. Second, in the adult zebrafish pallium, miR-9 is exclusively expressed in qNSCs and maintains this cell state, which differs from the embryonic situation where miR-9 is expressed in proliferating NPCs and favors neurogenic activity (Bonev et al., 2012; Coolen et al., 2012; Shibata et al., 2008). Finally, this functional change is associated with a modification of miR-9 subcellular localization. Indeed, whereas miR-9 is detected cytoplasmically in embryonic and juvenile NPCs, we unexpectedly observed a concentration of miR-9 inside the nucleus of qNSCs, in tight correlation with the presence of the effector Ago proteins (Figure 7A). Juvenile NPCs already display quiescence characteristics (Alunni et al., 2013; Dirian et al., 2014), thus, in addition to pinpointing an aged-dependent change in regulatory mechanisms of qNSCs, these data reinforce nuclear miR-9 expression as establishing a particular phase of the quiescence cycle, specific to mature NSCs. In the mouse DG, we observed an age-associated increase in the proportion of NSCs harboring miR-9 in their nucleus.

(D) Immunofluorescence for Ago2 (magenta) (left) and ISH for miR-9 (light blue) (right) and a nuclear DAPI counterstain (gray) on proliferating (top) and quiescent (bottom) adult hippocampal neural stem cells (AH-NSCs). Scale bars, 10 μm.

(E and F) Percentage of NSCs with high nuclear concentration of Ago2 (E) or miR-9 (F) in proliferation-promoting or quiescence-promoting conditions.

(G) Relative distribution of Ago2 (left) and miR-9 (right) signal intensities in the cytoplasm (dark gray) and nucleus (blue) in proliferating or quiescent NSCs; n = 15 confocal fields taken from 3 independent coverslips (5 fields/coverslip) in each condition; total proliferating NSCs = 2,411, total quiescent NSCs = 860.

However, at this point, because the temporal scales appear different, it remains an open question whether or not the same mechanisms are at play in the two species. Elucidating whether systemic factors are present that are capable of affecting miR-9 localization in an age-dependent fashion, or alternatively, if a NSC intrinsic clock could determine the switch of miR-9 preferential localization will shed more light on the mechanisms underlying the establishment and regulation of a mature NSC pool.

Although the canonical mechanism by which the Ago/RISC mediates gene expression is via mRNA silencing in the cytoplasm, several studies, largely performed in vitro, highlighted the presence of Ago complexes in the nucleus, although the precise mechanism of their shuttling is not fully understood (Nishi et al., 2013, 2015; Schraivogel and Meister, 2014; Schraivogel et al., 2015; Matsui et al., 2015). Here, we provide evidence for the active nuclear/cytoplasmic shuttling of Agos in vivo in NSCs, and moreover, we show that this transport depends on the interaction of Agos with TNRC6 proteins. Additionally, we observed a surprising specificity of nuclear Agos to the population of qNSCs expressing nuclear miR-9 thus revealing their interdependency and overall indicating that Ago complexes that translocate to the nucleus must be loaded with miR-9. As nuclear localization of miR-9 and Ago is specific to qNSCs, and more precisely to a subset of qNSCs at any given time, it would be interesting to resolve how their nuclear/cytoplasmic shuttling is regulated in concert with the cell-cycle status of these cells and potentially in response to environmental cues from the neurogenic niche. Additionally, in-depth analysis of other NSC-expressed microRNAs and nuclear RISC components will be important to define this regulatory pathway.

Some classes of small non-coding RNAs such as PIWI-interacting RNAs (piRNAs) and small interfering RNAs (siRNAs) are recognized as regulating gene expression in both the cytoplasm and nucleus, however, a potential regulatory role for microRNAs outside of the canonical cytoplasmic pathway has just started to be explored (Castel and Martienssen, 2013; Schraivogel and Meister, 2014). Moreover, whether their presence in the nucleus is functional or rather just a mechanism for passive storage is still heavily debated (Gagnon et al., 2014; Olejniczak et al., 2013). In this study, we show that the dynamic transport of Ago and miR-9 functionally influences the activation status of the cell. Specifically, trapping Ago/miR-9 in the cytoplasm increases NSCs activation rate, mimicking miR-9 kd phenotype. Conversely, increasing miR-9 and Agos nuclear concentration using LMB significantly decreased NSC activation, a phenotype that is reversed by blocking miR-9. Altogether, this data supports an active role for nuclear Ago/miR-9 complexes in qNSCs (Figure 7B). Interestingly, and in line with our results, in vitro studies have demonstrated that nuclear Ago/microRNA complexes repress the transcription of cell-cycle activators thus leading to cell-cycle arrest (Benhamed et al., 2012) opening to the intriguing possibility that an analogous nuclear Ago mechanism could be occurring in adult NSCs. Unravelling this mechanism and identifying miR-9/Ago targets in the nucleus will also shed light on the functional synergy between miR-9 and Notch signaling activity in the control of adult NSCs quiescence.

EXPERIMENTAL PROCEDURES

Animals

Wild-type (AB) and *Tg(gfap:gfp)*^{mi2001} (Bernardos and Raymond, 2006) zebrafish were maintained using standard protocols and in accordance with Institute Guidelines for Animal Welfare. All experiments performed on zebrafish conformed to the official standards of the Department of Essonne (agreement #A91-577). Three- to six-month-old adult fish were used for analysis unless otherwise stated. Mice were housed, bred, and treated according to the guidelines approved by the Home Office under the Animal (Scientific Procedures) Act 1986. All experimental procedures involving mice have been approved by the Animal Welfare and Ethical Review Panel of the National Institute for Medical Research.

BrdU Pulse-Chase and LY411575 Treatments

BrdU (1 mM, Sigma) was applied to the fish water at 28°C in the dark. Fish were subsequently transferred to a tank with fresh water during the chase period. LY411575 (10 μM, Stemgent) or DMSO carrier alone (0.4%–0.5%) was applied to the fish water for 48 hr at 28°C in the dark and refreshed once after 24 hr.

Ventricular Micro-injections and Electroporation

Micro-injections into the adult pallial ventricle were performed on anaesthetized fish as described (Rothenaigner et al., 2011). vivoMOs (Gene-tools) were injected at a concentration of 50 μM (Table S1). Leptomycin B (Sigma) was resuspended in MeOH and fish were injected with either 2.0 nL of 100 nM LMB or MeOH (70%) and brains were analyzed 1 dpi. For electroporation, plasmid DNA was diluted to 2–4 μg/μL in TE pH8.0 and injected into the ventricle. Fish were then administered two electric pulses (70 V, 50 ms width, 1,000 ms space). For epistasis experiments, electroporation was carried out 2 hr prior to vivoMO injections.

In Situ Hybridization

Adult zebrafish brains or embryos were fixed in 4% paraformaldehyde (PFA) overnight at 4°C. Mice were transcardially perfused with saline followed by 4% PFA and brains were dissected and postfixed with 4% PFA for 2 hr at 4°C. In situ hybridization (ISH) with DIG-labeled RNA probes were performed as described (Alunni et al., 2013). MicroRNA ISH using LNA probes (Exiqon) was performed according to Leucht et al. (2008) on zebrafish embryos and on free-floating vibratome sections of the zebrafish adult telencephalon or mouse brain. MicroRNA ISH using the LNA 2′-O-Me modified probes (Ribotask) was performed on 50 μm free-floating vibratome sections following manufacturer instructions. miR-9 ISH on cultured mouse cells was performed as described (Lu and Tsourkas, 2009). All in situs were revealed using fast red (Sigma) or NBT/BCIP (Sigma). ISH probes are listed in Table S2.

Immunohistochemistry

Fluorescent immunohistochemistry on zebrafish brain sections was performed as described (Chapouton et al., 2010). Perfused mouse adult brain tissue was sectioned coronally at 40 μm with a vibratome and subsequent immunohistochemistry was performed as described (Andersen et al., 2014). Immunohistochemistry on AH-NSCs was performed as described (Martynoga et al., 2013). The primary antibodies used in this study are listed in Table S3. For BrdU and PCNA staining, sections were incubated in either 2 N HCL for 30 min at 37°C or 1× HistoVT One (Nacalai Tesque) for 1 hr at 65°C. Goat or donkey secondary antibodies coupled to AlexaFluor dyes (Invitrogen) or Cy3/Cy5 dyes (Jackson Labs) were used (1:1,000) with DAPI (5 μg/μL) counterstain for nuclei.

qRT-PCR

Total RNA enriched for small RNAs were extracted from adult telencephali (pool of 4), 1 month post-fertilization whole brains (pool of 5), and whole embryos (pool of 50–100) using the High Pure miRNA Isolation Kit (Roche). The following reagents were used for detection of the primiR-9 transcripts: Superscript II kit (Invitrogen) with Random Hexamer Primers (Thermo Scientific) for cDNA synthesis and LightCycler FastStart DNA Master SYBR Green I (Roche) for qRT-PCR. Primers used for qRT-PCR are listed in Table S4. Efficiencies of each primer pair was evaluated by performing a dilution series

experiment. The following reagents were used for detection of mature miRs: miRCURY LNA Universal cDNA Synthesis Kit (Exiqon) for cDNA synthesis and miRCURY LNA ExiLENT SYBR Green master mix (Exiqon) for qRT-PCR. For each transcript/miR, two biological and two technical replicates were performed using the LightCycler 2.0 Carousel-Based System (Roche). Crossing points were calculated using the LightCycler 4.0 software (Roche) (normalized to β-*actin* and *gapdh* for the primary transcripts and *U6* for the mature miRs) and all relative expression analysis was done using the REST (Pfaffl et al., 2002) software tool that determines significant differences between control and sample groups-based crossing points using a randomization algorithm.

AH-NS Cell Culture

AH-NSCs were isolated from 6-week-old C57Bl6 mice using the neural tissue dissociation kit (Miltenyi Biotec) and cultured as described previously (Martynoga et al., 2013). Briefly, cells were plated at a density of 30,000 cells/cm^2 onto laminin coated coverslips (2 μg/mL) in normal NSC proliferation medium (EGF and FGF at 20 ng/mL; Peprotech). To induce quiescence, fresh NSC medium without EGF and with 20 ng/mL BMP4 (R&D Systems) was added. BMP4 containing media was changed daily. Cells were fixed in 4% PFA for 10 min.

Imaging, Cell Counting, and Statistics

Images were taken using a Zeiss LSM700 (Zeiss) confocal microscope using 20×, 40× (oil), or 63× (oil) objectives. Images were processed using the ZEN (Zeiss) and Fiji software. Cell counts on zebrafish brains were carried out manually on 50 μm z stacks from three serial sections from telencephali with n = 3 telencephali per condition unless otherwise stated. Imaris (Bitplane-Oxford Instruments) was used for all mouse DG cell counts. Briefly, spots were added automatically in the Sox2 channel to identify all Sox2$^+$ cells. To determine nuclear miR-9, a filter was added to the spots identifying Sox$^+$ cells based on the center intensity of the miR-9 channel. A center intensity of >55 was determined to be nuclear miR-9 expression. Analysis of Ago2 and miR-9 expression in AH-NSCs was carried out using the Fiji/ImageJ software. The subcellular distribution of Ago2 and miR-9 was analyzed using the Intensity Ration Nuclei Cytoplasm Tool plugin. For all analyses, n = 3 independent wells per sample with five confocal fields analyzed per well. For all quantitative experiments, statistical analysis was carried out using Excel and InVivoStat (Clark et al., 2012). Experimental data are expressed as means ± 95% confidence interval. Associations were determined using χ^2 tests for association. Comparisons between groups were made using one-way ANOVAs followed by Bonferroni post hoc correction.

SUPPLEMENTAL INFORMATION

Supplemental Information includes Supplemental Experimental Procedures, seven figures, and four tables and can be found with this article online at http://dx.doi.org/10.1016/j.celrep.2016.09.088.

AUTHOR CONTRIBUTIONS

S.K., M.C., and D.C. designed and performed experiments. N.U. and F.G. provided mouse reagents, designed experiments, and provided advice on the project. M.C. and L.B.-C. supervised the project. S.K., L.B.-C., and M.C. prepared the manuscript.

ACKNOWLEDGMENTS

We thank members of the ZEN lab and Eric Miska for their critical input. We are grateful to J. Ninkovic for the 4C4 antibody. Work in the L.B.-C. lab was funded by the EU project ZF-Health (FP7/2010-2015 grant agreement 242048), the ANR (grant ANR-2012-BSV4-0004-01), the Ecole des Neurosciences de Paris (ENP), the FRM (FRP "Equipe" DEQ20120323692), and the European Research Council (AdG 322936). M.C. is supported by INSERM. S.K. was recipient of fellowships from the ENP, the DIM Cerveau et Pensée of Région Ile de France, and The Company of Biologists Limited (Travelling Fellowship DEVTF-140404). N.U. was supported by the BBSRC (BB/K005316/1). Work in F.G.'s lab was supported by The Francis Crick Institute that receives its core funding from Cancer Research UK (FC001089), the UK Medical Research Council (FC001089), and the Wellcome Trust (FC001089).

Received: April 15, 2016
Revised: July 7, 2016
Accepted: September 26, 2016
Published: October 25, 2016

REFERENCES

Adolf, B., Chapouton, P., Lam, C.S., Topp, S., Tannhäuser, B., Strähle, U., Götz, M., and Bally-Cuif, L. (2006). Conserved and acquired features of adult neurogenesis in the zebrafish telencephalon. Dev. Biol. *295*, 278–293.

Alunni, A., Krecsmarik, M., Bosco, A., Galant, S., Pan, L., Moens, C.B., and Bally-Cuif, L. (2013). Notch3 signaling gates cell cycle entry and limits neural stem cell amplification in the adult pallium. Development *140*, 3335–3347.

Andersen, J., Urbán, N., Achimastou, A., Ito, A., Simic, M., Ullom, K., Martynoga, B., Lebel, M., Göritz, C., Frisén, J., et al. (2014). A transcriptional mechanism integrating inputs from extracellular signals to activate hippocampal stem cells. Neuron *83*, 1085–1097.

Bartel, D.P. (2009). MicroRNAs: target recognition and regulatory functions. Cell *136*, 215–233.

Benhamed, M., Herbig, U., Ye, T., Dejean, A., and Bischof, O. (2012). Senescence is an endogenous trigger for microRNA-directed transcriptional gene silencing in human cells. Nat. Cell Biol. *14*, 266–275.

Bernardos, R.L., and Raymond, P.A. (2006). GFAP transgenic zebrafish. Gene Expr. Patterns *6*, 1007–1013.

Bonev, B., Pisco, A., and Papalopulu, N. (2011). MicroRNA-9 reveals regional diversity of neural progenitors along the anterior-posterior axis. Dev. Cell *20*, 19–32.

Bonev, B., Stanley, P., and Papalopulu, N. (2012). MicroRNA-9 modulates Hes1 ultradian oscillations by forming a double-negative feedback loop. Cell Rep. *2*, 10–18.

Castel, S.E., and Martienssen, R.A. (2013). RNA interference in the nucleus: roles for small RNAs in transcription, epigenetics and beyond. Nat. Rev. Genet. *14*, 100–112.

Chapouton, P., Adolf, B., Leucht, C., Tannhäuser, B., Ryu, S., Driever, W., and Bally-Cuif, L. (2006). her5 expression reveals a pool of neural stem cells in the adult zebrafish midbrain. Development *133*, 4293–4303.

Chapouton, P., Skupien, P., Hesl, B., Coolen, M., Moore, J.C., Madelaine, R., Kremmer, E., Faus-Kessler, T., Blader, P., Lawson, N.D., and Bally-Cuif, L. (2010). Notch activity levels control the balance between quiescence and recruitment of adult neural stem cells. J. Neurosci. *30*, 7961–7974.

Cheung, T.H., and Rando, T.A. (2013). Molecular regulation of stem cell quiescence. Nat. Rev. Mol. Cell Biol. *14*, 329–340.

Cheung, T.H., Quach, N.L., Charville, G.W., Liu, L., Park, L., Edalati, A., Yoo, B., Hoang, P., and Rando, T.A. (2012). Maintenance of muscle stem-cell quiescence by microRNA-489. Nature *482*, 524–528.

Clark, R.A., Shoaib, M., Hewitt, K.N., Stanford, S.C., and Bate, S.T. (2012). A comparison of InVivoStat with other statistical software packages for analysis of data generated from animal experiments. J. Psychopharmacol. (Oxford) *26*, 1136–1142.

Codega, P., Silva-Vargas, V., Paul, A., Maldonado-Soto, A.R., Deleo, A.M., Pastrana, E., and Doetsch, F. (2014). Prospective identification and purification of quiescent adult neural stem cells from their in vivo niche. Neuron *82*, 545–559.

Coolen, M., Thieffry, D., Drivenes, Ø., Becker, T.S., and Bally-Cuif, L. (2012). miR-9 controls the timing of neurogenesis through the direct inhibition of antagonistic factors. Dev. Cell *22*, 1052–1064.

Coolen, M., Katz, S., and Bally-Cuif, L. (2013). miR-9: a versatile regulator of neurogenesis. Front. Cell. Neurosci. *7*, 220.

Crist, C.G., Montarras, D., and Buckingham, M. (2012). Muscle satellite cells are primed for myogenesis but maintain quiescence with sequestration of

Myf5 mRNA targeted by microRNA-31 in mRNP granules. Cell Stem Cell *11*, 118–126.

Dirian, L., Galant, S., Coolen, M., Chen, W., Bedu, S., Houart, C., Bally-Cuif, L., and Foucher, I. (2014). Spatial regionalization and heterochrony in the formation of adult pallial neural stem cells. Dev. Cell *30*, 123–136.

Encinas, J.M., Michurina, T.V., Peunova, N., Park, J.-H., Tordo, J., Peterson, D.A., Fishell, G., Koulakov, A., and Enikolopov, G. (2011). Division-coupled astrocytic differentiation and age-related depletion of neural stem cells in the adult hippocampus. Cell Stem Cell *8*, 566–579.

Eulalio, A., Huntzinger, E., and Izaurralde, E. (2008). GW182 interaction with Argonaute is essential for miRNA-mediated translational repression and mRNA decay. Nat. Struct. Mol. Biol. *15*, 346–353.

Flores, O., Kennedy, E.M., Skalsky, R.L., and Cullen, B.R. (2014). Differential RISC association of endogenous human microRNAs predicts their inhibitory potential. Nucleic Acids Res. *42*, 4629–4639.

Gagnon, K.T., Li, L., Chu, Y., Janowski, B.A., and Corey, D.R. (2014). RNAi factors are present and active in human cell nuclei. Cell Rep. *6*, 211–221.

Ganz, J., Kaslin, J., Hochmann, S., Freudenreich, D., and Brand, M. (2010). Heterogeneity and Fgf dependence of adult neural progenitors in the zebrafish telencephalon. Glia *58*, 1345–1363.

Giachino, C., and Taylor, V. (2014). Notching up neural stem cell homogeneity in homeostasis and disease. Front. Neurosci. *8*, 32.

Grandel, H., Kaslin, J., Ganz, J., Wenzel, I., and Brand, M. (2006). Neural stem cells and neurogenesis in the adult zebrafish brain: origin, proliferation dynamics, migration and cell fate. Dev. Biol. *295*, 263–277.

Hsieh, J. (2012). Orchestrating transcriptional control of adult neurogenesis. Genes Dev. *26*, 1010–1021.

Kizil, C., and Brand, M. (2011). Cerebroventricular microinjection (CVMI) into adult zebrafish brain is an efficient misexpression method for forebrain ventricular cells. PLoS ONE *6*, e27395.

Kizil, C., Kyritsis, N., Dudczig, S., Kroehne, V., Freudenreich, D., Kaslin, J., and Brand, M. (2012). Regenerative neurogenesis from neural progenitor cells requires injury-induced expression of Gata3. Dev. Cell *23*, 1230–1237.

Kloosterman, W.P., Lagendijk, A.K., Ketting, R.F., Moulton, J.D., and Plasterk, R.H.A. (2007). Targeted inhibition of miRNA maturation with morpholinos reveals a role for miR-375 in pancreatic islet development. PLoS Biol. *5*, e203.

Kroehne, V., Freudenreich, D., Hans, S., Kaslin, J., and Brand, M. (2011). Regeneration of the adult zebrafish brain from neurogenic radial glia-type progenitors. Development *138*, 4831–4841.

Kyritsis, N., Kizil, C., Zocher, S., Kroehne, V., Kaslin, J., Freudenreich, D., Iltzsche, A., and Brand, M. (2012). Acute inflammation initiates the regenerative response in the adult zebrafish brain. Science *338*, 1353–1356.

Leucht, C., Stigloher, C., Wizenmann, A., Klafke, R., Folchert, A., and Bally-Cuif, L. (2008). MicroRNA-9 directs late organizer activity of the midbrain-hindbrain boundary. Nat. Neurosci. *11*, 641–648.

Lim, D.A., and Alvarez-Buylla, A. (2014). Adult neural stem cells stake their ground. Trends Neurosci. *37*, 563–571.

Lu, J., and Tsourkas, A. (2009). Imaging individual microRNAs in single mammalian cells in situ. Nucleic Acids Res. *37*, e100.

Lugert, S., Basak, O., Knuckles, P., Haussler, U., Fabel, K., Götz, M., Haas, C.A., Kempermann, G., Taylor, V., and Giachino, C. (2010). Quiescent and active hippocampal neural stem cells with distinct morphologies respond selectively to physiological and pathological stimuli and aging. Cell Stem Cell *6*, 445–456.

Martynoga, B., Mateo, J.L., Zhou, B., Andersen, J., Achimastou, A., Urbán, N., van den Berg, D., Georgopoulou, D., Hadjur, S., Wittbrodt, J., et al. (2013). Epigenomic enhancer annotation reveals a key role for NFIX in neural stem cell quiescence. Genes Dev. *27*, 1769–1786.

März, M., Chapouton, P., Diotel, N., Vaillant, C., Hesl, B., Takamiya, M., Lam, C.S., Kah, O., Bally-Cuif, L., and Strähle, U. (2010). Heterogeneity in progenitor cell subtypes in the ventricular zone of the zebrafish adult telencephalon. Glia *58*, 870–888.

Matsui, M., Li, L., Janowski, B.A., and Corey, D.R. (2015). Reduced expression of Argonaute 1, Argonaute 2, and TRBP changes levels and intracellular distribution of RNAi factors. Sci. Rep. *5*, 12855.

Meister, G. (2013). Argonaute proteins: functional insights and emerging roles. Nat. Rev. Genet. *14*, 447–459.

Ming, G.L., and Song, H. (2011). Adult neurogenesis in the mammalian brain: significant answers and significant questions. Neuron *70*, 687–702.

Mira, H., Andreu, Z., Suh, H., Lie, D.C., Jessberger, S., Consiglio, A., San Emeterio, J., Hortigüela, R., Marqués-Torrejón, M.Á., Nakashima, K., et al. (2010). Signaling through BMPR-IA regulates quiescence and long-term activity of neural stem cells in the adult hippocampus. Cell Stem Cell *7*, 78–89.

Muñoz, D.M., Singh, S., Tung, T., Agnihotri, S., Nagy, A., Guha, A., Zadeh, G., and Hawkins, C. (2013). Differential transformation capacity of neuro-glial progenitors during development. Proc. Natl. Acad. Sci. USA *110*, 14378–14383.

Nam, J.-W., Rissland, O.S., Koppstein, D., Abreu-Goodger, C., Jan, C.H., Agarwal, V., Yildirim, M.A., Rodriguez, A., and Bartel, D.P. (2014). Global analyses of the effect of different cellular contexts on microRNA targeting. Mol. Cell *53*, 1031–1043.

Nelson, P.T., De Planell-Saguer, M., Lamprinaki, S., Kiriakidou, M., Zhang, P., O'Doherty, U., and Mourelatos, Z. (2007). A novel monoclonal antibody against human Argonaute proteins reveals unexpected characteristics of miRNAs in human blood cells. RNA *13*, 1787–1792.

Nishi, K., Nishi, A., Nagasawa, T., and Ui-Tei, K. (2013). Human TNRC6A is an Argonaute-navigator protein for microRNA-mediated gene silencing in the nucleus. RNA *19*, 17–35.

Nishi, K., Takahashi, T., Suzawa, M., Miyakawa, T., Nagasawa, T., Ming, Y., Tanokura, M., and Ui-Tei, K. (2015). Control of the localization and function of a miRNA silencing component TNRC6A by Argonaute protein. Nucleic Acids Res. *43*, 9856–9873.

Olejniczak, S.H., La Rocca, G., Gruber, J.J., and Thompson, C.B. (2013). Long-lived microRNA-Argonaute complexes in quiescent cells can be activated to regulate mitogenic responses. Proc. Natl. Acad. Sci. USA *110*, 157–162.

Pfaffl, M.W., Horgan, G.W., and Dempfle, L. (2002). Relative expression software tool (REST) for group-wise comparison and statistical analysis of relative expression results in real-time PCR. Nucleic Acids Res. *30*, e36.

Rissland, O.S., Hong, S.-J., and Bartel, D.P. (2011). MicroRNA destabilization enables dynamic regulation of the miR-16 family in response to cell-cycle changes. Mol. Cell *43*, 993–1004.

Rothenaigner, I., Krecsmarik, M., Hayes, J.A., Bahn, B., Lepier, A., Fortin, G., Götz, M., Jagasia, R., and Bally-Cuif, L. (2011). Clonal analysis by distinct viral vectors identifies bona fide neural stem cells in the adult zebrafish telencephalon and characterizes their division properties and fate. Development *138*, 1459–1469.

Sato, T., Yamamoto, T., and Sehara-Fujisawa, A. (2014). miR-195/497 induce postnatal quiescence of skeletal muscle stem cells. Nat. Commun. *5*, 4597.

Schraivogel, D., and Meister, G. (2014). Import routes and nuclear functions of Argonaute and other small RNA-silencing proteins. Trends Biochem. Sci. *39*, 420–431.

Schraivogel, D., Schindler, S.G., Danner, J., Kremmer, E., Pfaff, J., Hannus, S., Depping, R., and Meister, G. (2015). Importin-β facilitates nuclear import of human GW proteins and balances cytoplasmic gene silencing protein levels. Nucleic Acids Res. *43*, 7447–7461.

Shibata, M., Kurokawa, D., Nakao, H., Ohmura, T., and Aizawa, S. (2008). MicroRNA-9 modulates Cajal-Retzius cell differentiation by suppressing Foxg1 expression in mouse medial pallium. J. Neurosci. *28*, 10415–10421.

Shibata, M., Nakao, H., Kiyonari, H., Abe, T., and Aizawa, S. (2011). MicroRNA-9 regulates neurogenesis in mouse telencephalon by targeting multiple transcription factors. J. Neurosci. *31*, 3407–3422.

Søe, M.J., Møller, T., Dufva, M., and Holmstrøm, K. (2011). A sensitive alternative for microRNA in situ hybridizations using probes of 2′-O-methyl RNA + LNA. J. Histochem. Cytochem. *59*, 661–672.

Suh, H., Consiglio, A., Ray, J., Sawai, T., D'Amour, K.A., and Gage, F.H. (2007). In vivo fate analysis reveals the multipotent and self-renewal capacities of Sox2+ neural stem cells in the adult hippocampus. Cell Stem Cell *1*, 515–528.

Takke, C., Dornseifer, P., v Weizsacker, E., and Campos-Ortega, J.A. (1999). her4, a zebrafish homologue of the Drosophila neurogenic gene E(spl), is a target of NOTCH signalling. Development *126*, 1811–1821.

Than-Trong, E., and Bally-Cuif, L. (2015). Radial glia and neural progenitors in the adult zebrafish central nervous system. Glia *63*, 1406–1428.

Urbán, N., and Guillemot, F. (2014). Neurogenesis in the embryonic and adult brain: same regulators, different roles. Front. Cell. Neurosci. *8*, 396.

Wang, D., Zhang, Z., O'Loughlin, E., Wang, L., Fan, X., Lai, E.C., and Yi, R. (2013). MicroRNA-205 controls neonatal expansion of skin stem cells by modulating the PI(3)K pathway. Nat. Cell Biol. *15*, 1153–1163.

Wienholds, E., Kloosterman, W.P., Miska, E., Alvarez-Saavedra, E., Berezikov, E., de Bruijn, E., Horvitz, H.R., Kauppinen, S., and Plasterk, R.H.A. (2005). MicroRNA expression in zebrafish embryonic development. Science *309*, 310–311.

Zhao, C., Sun, G., Li, S., and Shi, Y. (2009). A feedback regulatory loop involving microRNA-9 and nuclear receptor TLX in neural stem cell fate determination. Nat. Struct. Mol. Biol. *16*, 365–371.

Cell Reports, Volume *17*

Supplemental Information

A Nuclear Role for miR-9 and Argonaute Proteins in Balancing Quiescent and Activated Neural Stem Cell States

Shauna Katz, Delphine Cussigh, Noelia Urbán, Isabelle Blomfield, François Guillemot, Laure Bally-Cuif, and Marion Coolen

Supplemental Information

Supplemental Figures and Legends

Figure S1, Related to Figure 1

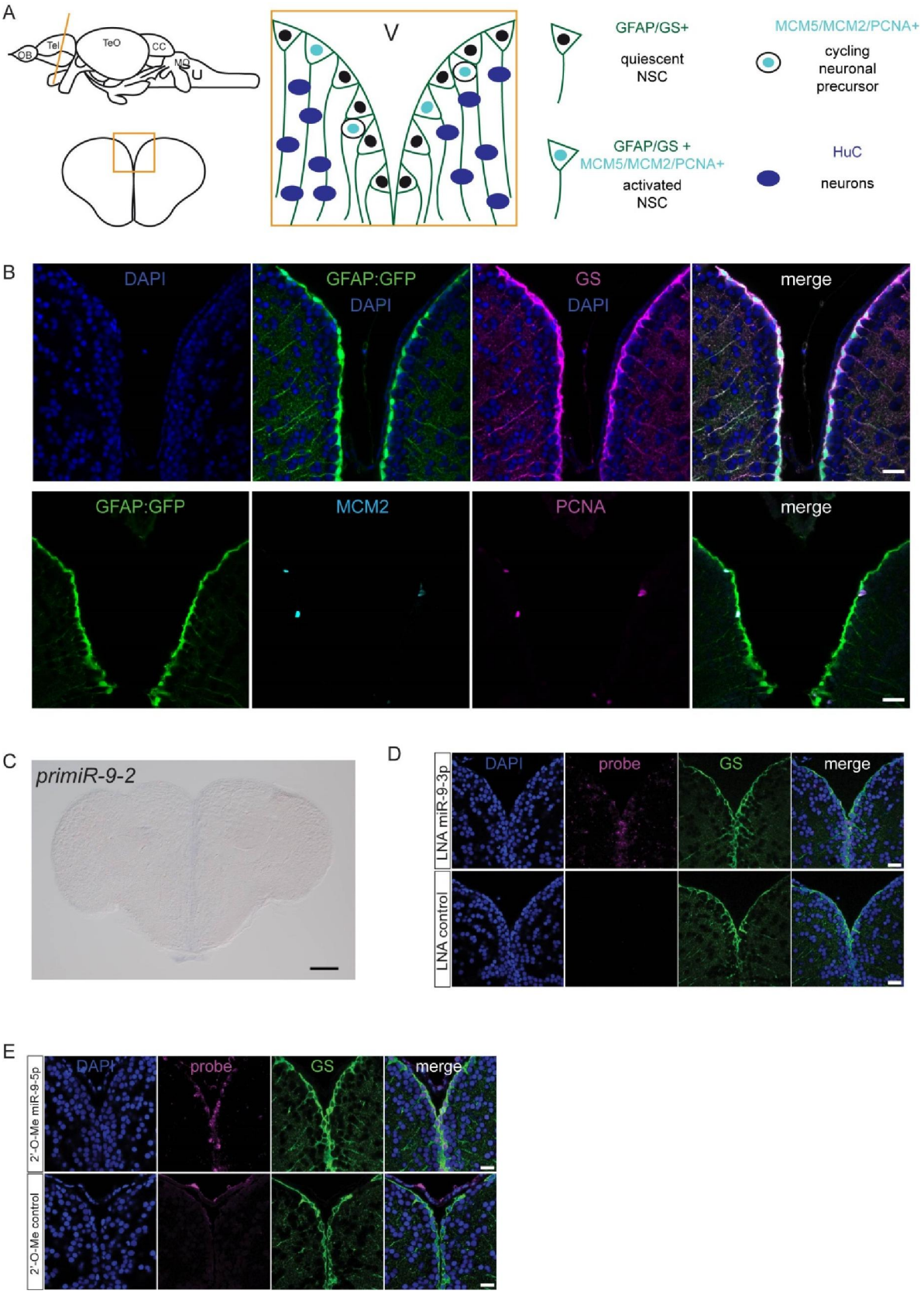

Figure S2, Related to Figure 2

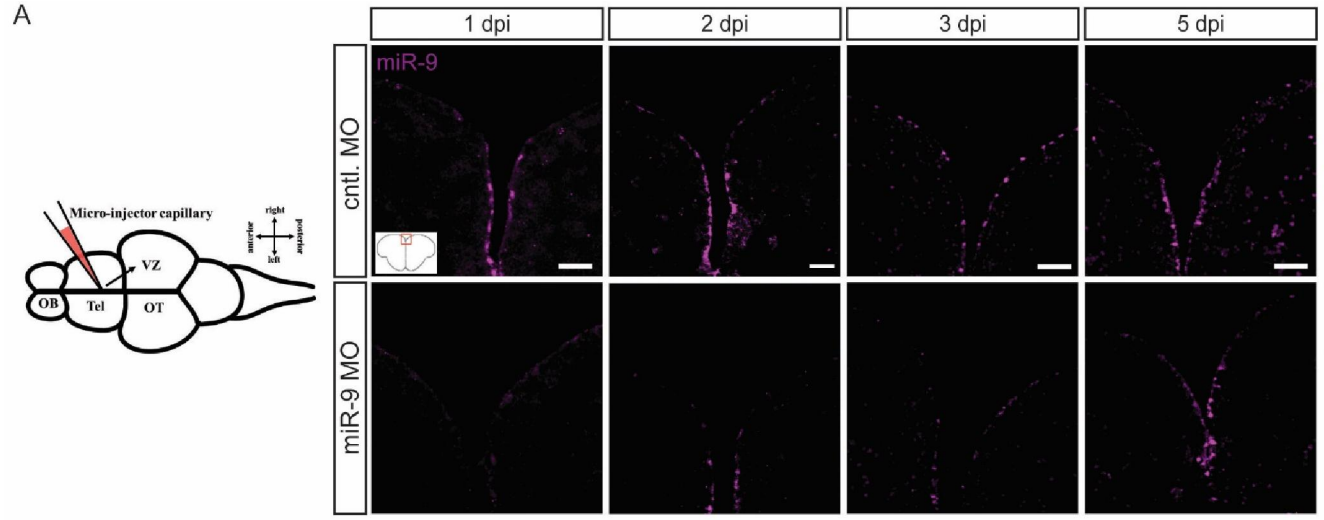

B

	number of mismatches						
	9.1	9.2	9.3	9.4	9.5	9.6	9.7
Processing MO1	0	0	3	2	0	1	2
Processing MO6	3	3	3	3	2	0	3

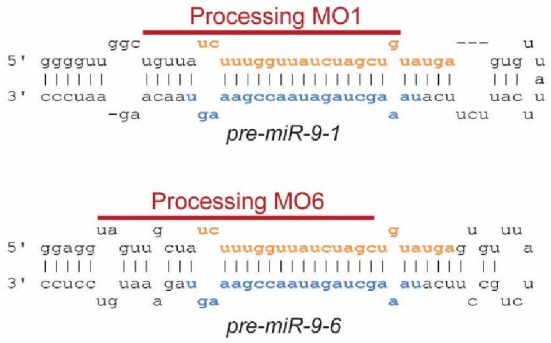

C

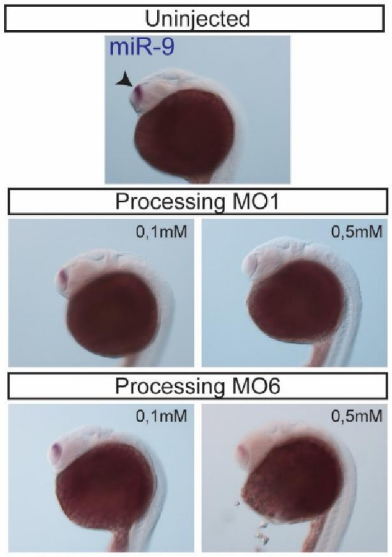

D

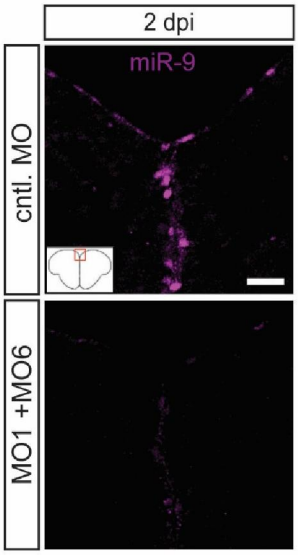

E

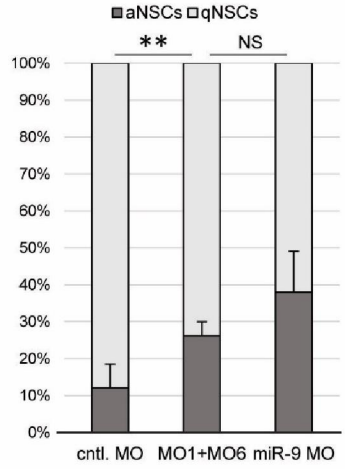

F

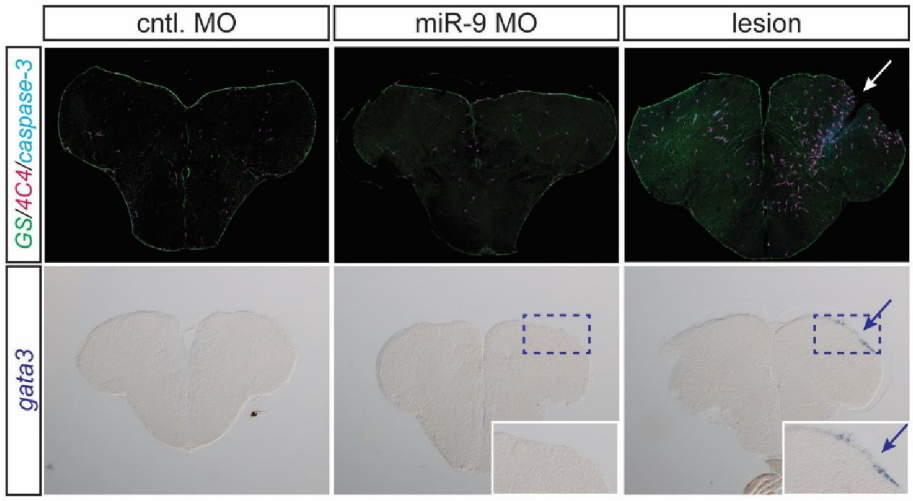

Figure S3, Related to Figure 3

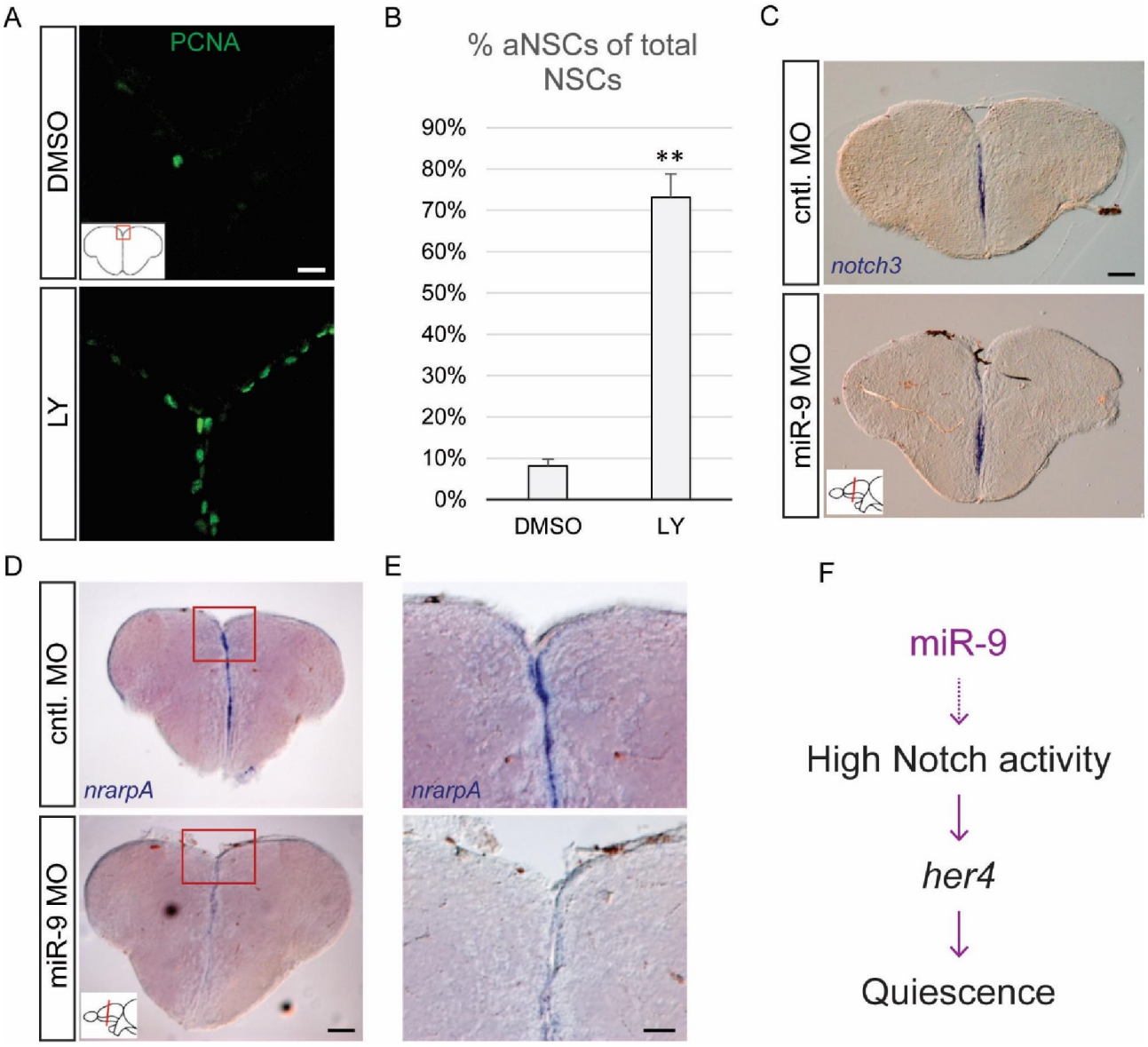

Figure S4, Related to Figure 4

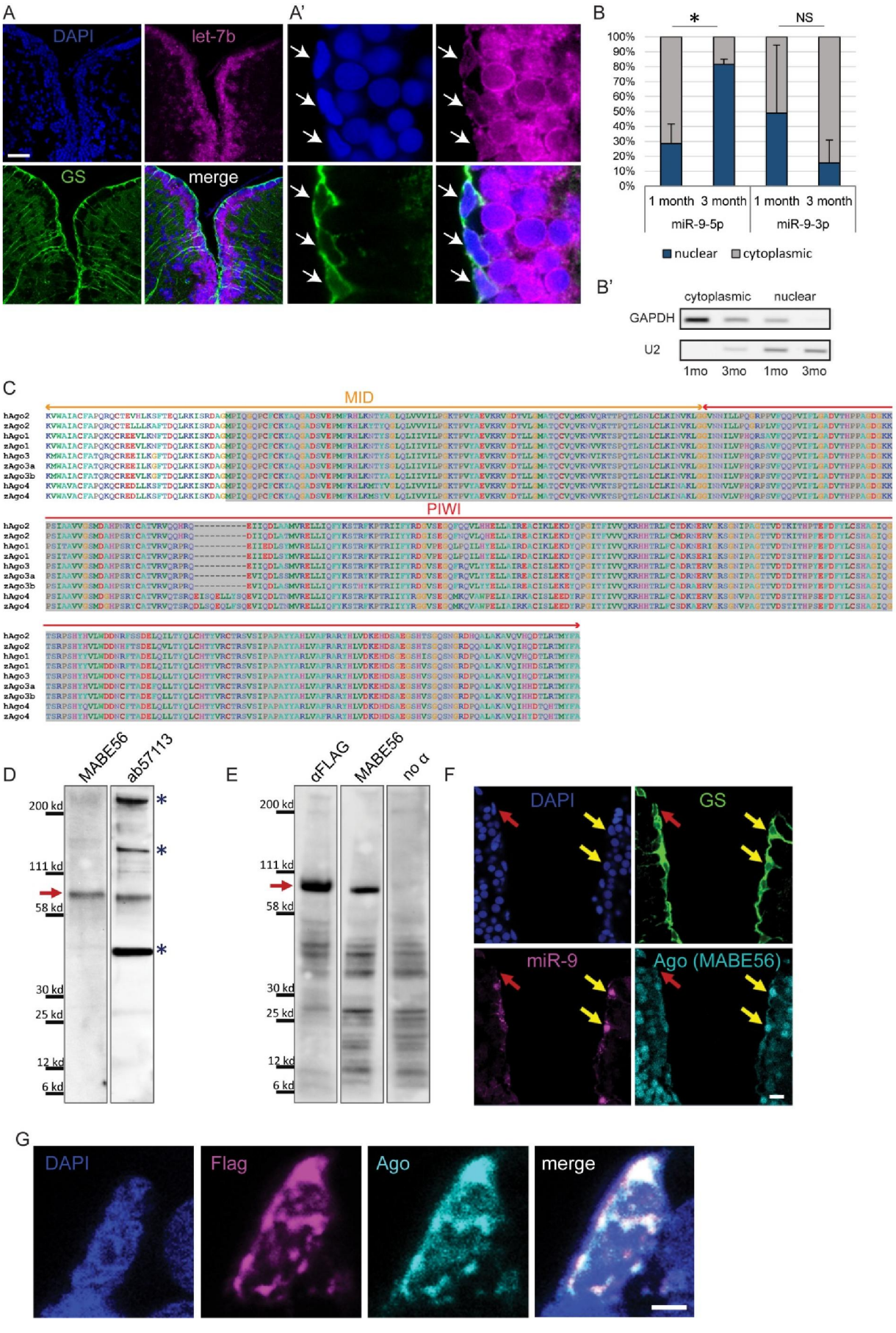

Figure S5, Related to Figure 4

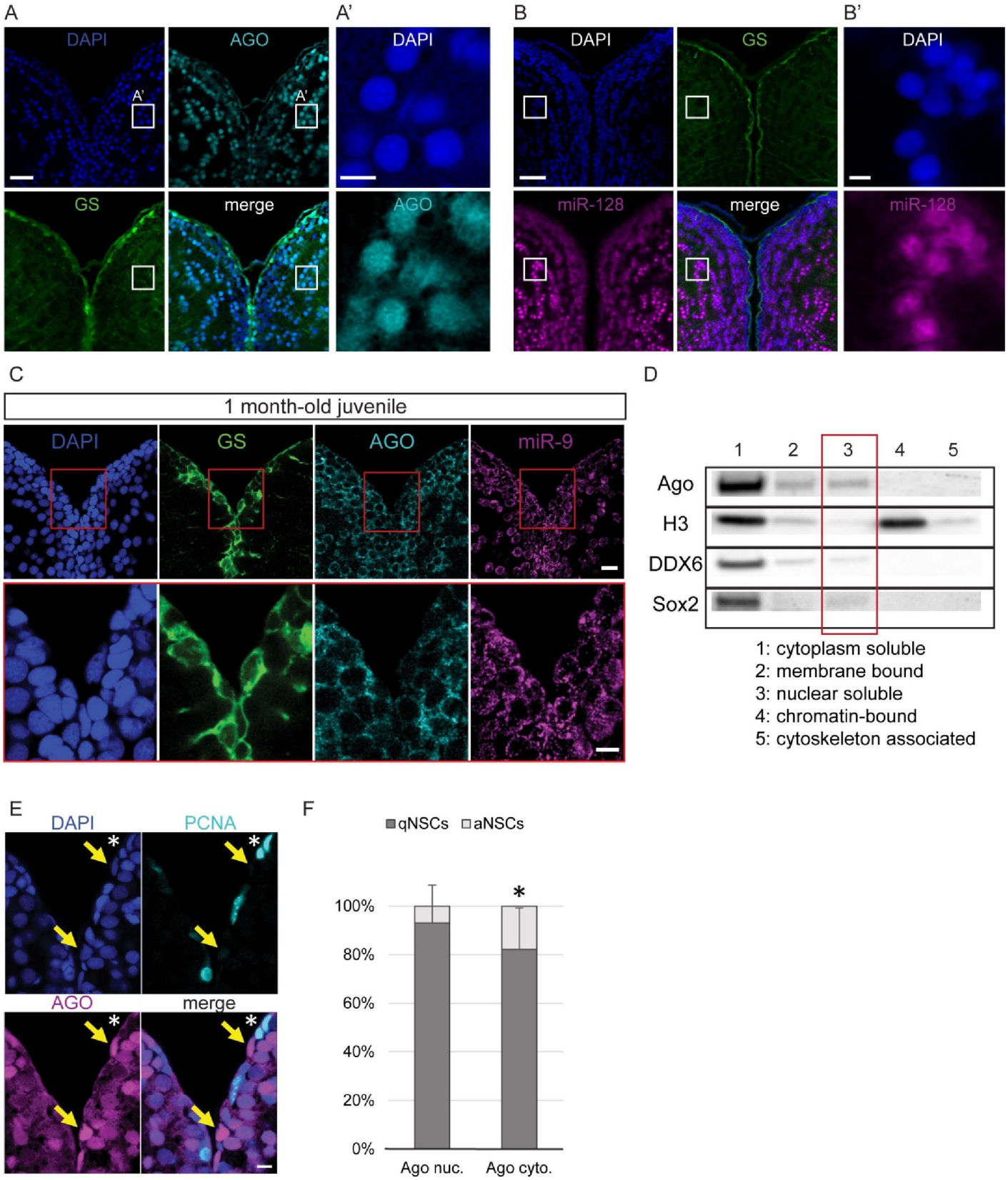

Figure S6, Related to Figure 5

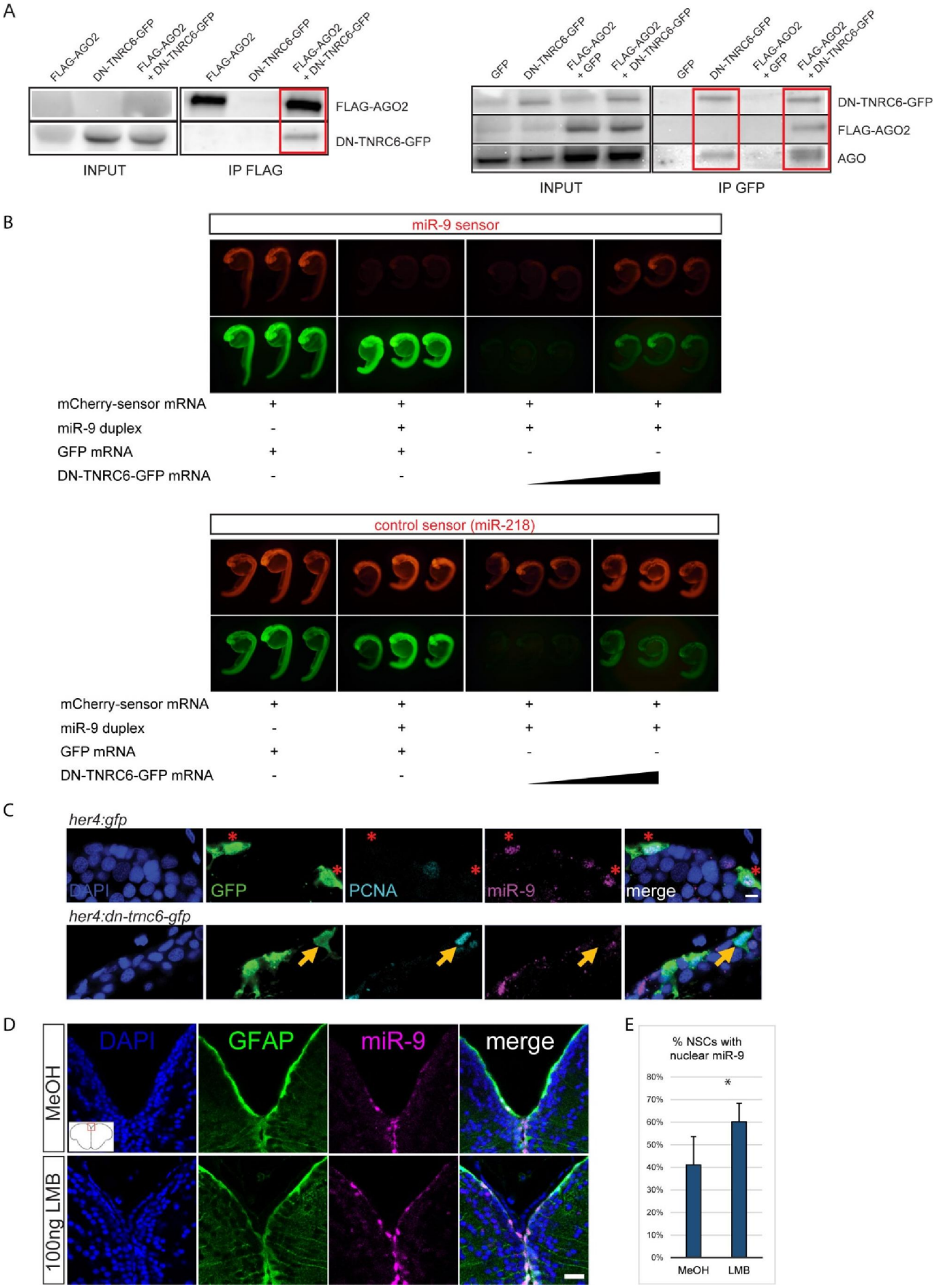

Figure S7, Related to Figure 6

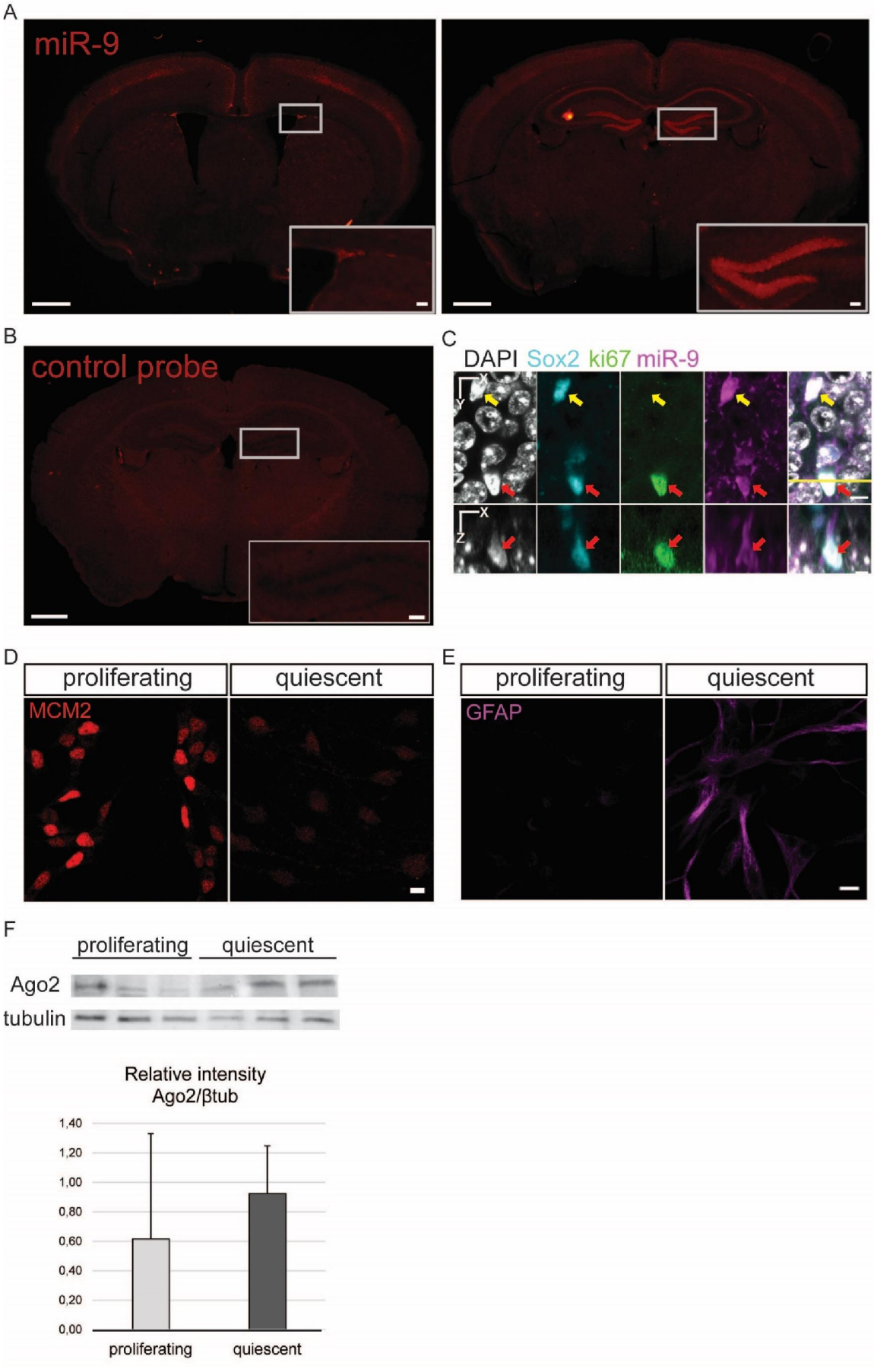

Supplemental figure legends

Figure S1. Validation of markers and of the specificity of the LNA miR-9 probe, related to figure 1

(**A**) Schematic representation of the germinal zone of the adult zebrafish pallium. Radial glia cells (GFAP+/GS+) lining the ventricle are *bona fide* NSCs and can be found in two states: activated or quiescent. The activated state is defined by the expression of proliferation markers (MCM2/MCM5/PCNA). Once activated, NSCs give rise to non-glial intermediate precursors which are committed towards neuronal differentiation. (**B**) Validation of the markers used in this study. All radial glia NSCs co-express GFP driven by the *gfap* promoter (green, *gfap*:GFP) and GS (magenta) (top panel). A small fraction of NSCs are found in an activated state in which they co-express proliferation markers (MCM2, light blue; PCNA, magenta) (bottom panel). Scale bars=50µm (**C**) ISH of pri-miR-9-2 demonstrating that it is not expressed in the adult telencephalon. Scale Scale bar=100µm. (**D**) ISH using LNA probes for miR-9-3p (magenta, top panel) and a control sequence (magenta, bottom panel) with immunofluorescence for GS (green) and nuclear DAPI counterstaining (dark blue) demonstrating the specificity of the LNA probes used for mature miR-9-5p detection. In contrast to miR-9-5p, miR-9-3p expression is much fainter and more diffuse although it is present at very low levels in the nucleus of some ventricular NSCs. (**E**) ISH using LNA 2'-O-Me probes for miR-9-5p (magenta, top panel) and a control sequence (magenta, bottom panel) with immunofluorescence for GS (green) and nuclear DAPI counterstaining (dark blue) confirming the exclusive expression of miR-9-5p in the ventricular NSCs. Scale bars=20µm.

Figure S2. Validation of the specificity of the effect of miR-9 knock-down on NSCs, related to figure 2

(**A**) ISH using a miR-9 LNA probe (magenta) demonstrating efficient knock-down of miR-9 at 1, 2, 3 and 5dpi of the miR-9 vivoMO (bottom panel) when compared with the control vivoMO (bottom panel). Note that at 5dpi the vivoMO no longer has any effect. Scale bar=20µm. (**B**) Design of processing morpholinos. The table on the top displays the number of mismatches between the two morpholinos (MO1 and MO6) and the 7 different pre-miR-9 hairpins. The morpholinos were designed to efficiently target premiR-9 hairpins which are the most expressed in adult brains. Below, the two drawings present the target position of the two morpholinos around the Drosha processing sites on premiR-9-1 and pre-miR-9-6 hairpins. (**C**) ISH with miR-9 LNA probe (blue) showing effective knock-down of miR-9 by the processing morpholinos MO1 and MO6 injected in the zebrafish embryo at different doses (0.1mM and 0.5mM). At 24 hours post-fertilization (hpf), miR-9 is expressed in the embryonic telencephalon as seen in control embryos (top panel, arrowhead; Leucht et al., 2008). The processing morpholinos induce a dose-dependent decrease in mature miR-9 production (bottom panels). (**D**) ISH using a miR-9 LNA probe (magenta) demonstrating efficient knock-down of miR-9 at 2dpi of the processing vivoMOs into the adult brain ventricle (bottom panel) when compared with the control vivoMO (bottom panel). Scale bar=20µm. (**E**) Percentage of aNSCs (dark grey) and qNSCs (light grey) 2dpi of control vivoMO, processing vivoMOs or miR-9 vivoMO demonstrating significant increase in aNSCs. n=3 brains per condition; data are represented as mean ± 95% CI. (*) $p<0.05$, (**) $p<0.01$; one-way ANOVA with Bonferroni post-hoc correction (**F**) Immunostaining for GS (green), 4C4 anti-fish leukocytes (magenta) and cleaved caspase-3 (cyan) (top panels) and ISH with a *gata3* probe (blue, bottom panels) following vivoMOs injections or a stab-wound lesion as a control of the stainings. No overt sign of acute inflammation or increased apoptosis is seen unpon vivoMO injections.

Figure S3. Validation of efficient Notch blockade and effects of miR-9 knock-down on Notch target genes, related to figure 3

(**A**) Fluorescent immunostaining of PCNA (green) after 48h of Notch inhibition with LY (bottom panel) or the DMSO control (top panel). Scale bar= 20µm. (**B**) Percentage of activated NSCs (PCNA+/GFAP+) upon LY vs DMSO treatment. n=3 brains per condition; data are represented as mean ± 95% CI. (**) $p<0.01$; one-way ANOVA with Bonferroni post-hoc correction. (**C-E**) ISH using specific probes for *notch3*(**C**) and *nrarpA* (**D, E**) 2dpi with the miR-9 MO (bottom panels) or control MO (top panels). Scale bars=100µm (C, D) or 40µm (E). (**F**) Proposed mechanism of action of miR-9 on quiescence, through potentiating Notch activity in NSCs.

Figure S4. Confirmation of specific subcellular localization of miR-9 and validation of Ago antibodies (ab57113 and MABE56), related to figure 4

(**A-A'**) ISH using LNA probe for let-7b (magenta) combined with immunostaining for GS (green) and DAPI counterstaining (dark blue). In the zebrafish pallium let-7b expression is localized to the first ventricular raws of cells (A); in NSCs (white arrows) let-7b ISH signal is restricted to the cytoplasm (A'). Scale bars=50µm (A) and 5µm (A') (**B-B'**) RT-qPCR analysis of miR-9 levels in fractionated RNA samples. (**B**) Nucleo-cytoplasmic ratio of miR-9 and miR-9-3p levels based on qPCR analysis on fractionated samples from the juvenile (1 month-old) and adult (3 months-old) zebrafish telencephalon. n=2 biological replicates per sample; data are represented as mean ± SEM. (*) $p<0.05$; t-tailed t-test after arcsin transformation. (**B'**) Control of the purity of the cytoplasmic and nuclear fractions by PCR using *GAPDH* and *U2* specific primers. (**C**) Alignment of MID and PIWI domains of Argonaute proteins from human and zebrafish. In these regions Ago proteins (1-4) sequences are highly conserved between human and zebrafish. The Ago antibody ab57113 was raised against a highly conserved portion of the C-terminal region of human Ago2 spanning the PIWI and part of the MID domains (residues 483-859; highlighted in grey). The second Ago antibody (pan-Ago MABE56) was raised against human Ago2 residues 47-859, and the epitope located to the C-terminal region. (**D**) Western blot analysis of adult telencephalic extracts using the two different Ago antibodies (MABE56, exposure time=5 min; ab57113, exposure time=2 min.). Red arrow indicates that both antibodies detect the Ago specific band at ~96 kd (blue asterisks indicate non-specific bands). (**E**) Western blot analysis of protein extracts from embryos injected with Flag-tagged zebrafish Ago2 using an anti-Flag antibody (exposure time=1 min.), Ago antibody (MABE56, exposure time=5 min.) and a no primary antibody control showing non-specific bands (exposure time=2 min.). Red arrow indicates the specific Ago band at ~96 kd detected by both the anti-Flag and anti-Ago antibodies. (**F**) ISH for miR-9 (magenta) and double immunofluorescence of GS (green) and Ago (MABE56, light blue) with nuclear DAPI counterstaining (dark blue). As with the ab57113 anti-Ago antibody (Figure 4D), the

signal for Ago is nuclear only in the miR-9+ NSCs (yellow arrows) and not in the miR-9- NSCs (red arrow), thus validating the specific detection of Ago proteins using these antibodies. Scale bar=20µm. (**G**) Representative picture of a ventricular NSC electroporated with Ago2-Flag. Double immunofluorescence of Flag (magenta) and Ago (ab57113, light blue) with nuclear DAPI counterstain (dark blue) demonstrates that the expression of Ago as detected by the Ago antibody overlaps with the expression of the Flag-tagged Ago2 further validating the specificity of the Ago antibody. Notably, Ago2-Flag foci are detected in the nucleus of the electroporated cell. Scale bar=2µm.

Figure S5. Nuclear localization of Argonaute proteins in the adult zebrafish pallium and its association with quiescence in mature NSCs, related to figure 4

(**A-A'**) Fluorescent immunodetection of Ago (light blue), GS (green), with DAPI counterstaining (dark blue). A' is a zoom on the region indicated by a white square in A, showing a strong nuclear staining for AGO in some parenchymal neurons (**B-B'**) ISH using a LNA probe for miR-128 (magenta) combined with immunostaining for GS (green) and DAPI counterstaining (dark blue). B' is a zoom on the region indicated by a white square in B, showing a strong nuclear staining for miR-128 in some parenchymal neurons. Scale bars=20µm (A,B) and 5µm (A',B') (**C**) Sections through the medial region of the dorsal telencephalon of a 1mpf juvenile fish showing ISH of miR-9 (magenta) and double immunofluorescence of GS (green) and Ago (light blue) with nuclear DAPI counterstaining (dark blue) demonstrating that miR-9 and Ago are located exclusively in the cytoplasm of the RG progenitors. Scale bars=10µm. (**D**) Western blot analysis of fractionated proteins samples from the adult zebrafish telencephalon. Substantial levels of Ago proteins can be detected in the nuclear soluble fraction (lane 3). (**E**) Double immunofluorescence of PCNA (light blue) and Ago (magenta) with a nuclear DAPI counterstaining (dark blue) illustrating that strong nuclear Ago is never in PCNA+ aNSCs (yellow arrows) and aNSCs express Ago in the cytoplasm (white asterisk). Scale bar=10µm. (**F**) Proportion of qNSCs (*gfap*+, MCM5-; dark grey) and aNSCs (*gfap*+, MCM5-; light grey) among NSCs with mostly nuclear (Ago nuc.) or cytoplasmic Ago (Ago cyto.) demonstrating an association between nuclear Ago and quiescence (χ^2 p-value<0.01). n=3 brains; data are represented as mean ± 95% CI.

Figure S6. Validation of the DN-TNRC6 construct and effect of DN-TNRC6 and LMB on miR-9, related to figure 5

(**A**) Co-immunoprecipitation experiments between DN-TNRC6-GFP and AGO proteins. Zebrafish embryos were injected with combinations of GFP-, FLAG-AGO2- or DN-TNRC6-GFP-encoding capped mRNA and subjected to immunoprecipitation with anti-FLAG beads (left panel) or anti-GFP beads (right panels). Input samples (1/10) and co-immunoprecipitated samples were then subjected to Western blot with antibodies for GFP, FLAG or AGO. DN-TNRC6-GFP co-immunoprecipitates with FLAG-AGO2 (right panel), and both FLAG-AGO2 and endogenous AGO proteins can be co-immunoprecipitated with DN-TNRC6-GFP (left panels). (**B**) miR-9 sensor assays in the presence of DN-TNRC6-GFP. mCherry sensor mRNAs harbouring binding sites for miR-9 (top panel) or miR-218 (bottom panel) were injected in zebrafish eggs together with miR-9 duplexes, GFP mRNA or DN-TNRC6-GFP mRNA at increasing doses. Embryos were imaged at 24hpf and a picture of 3 representative embryos is shown for each condition. miR-9 duplexes efficiently silence miR-9 sensor expression, while having no effect on the control miR-218 sensor. High doses of DN-TNRC6-GFP mRNA induce a specific rescue of miR-9-induced silencing of the miR-9 sensor. (**C**) ISH for miR-9 (magenta) and double immunofluorescence of GFP (green) and PCNA (light blue) with nuclear DAPI counterstaining (dark blue) demonstrating that cells electroporated with the DN-TNRC6 construct (bottom panel) never display nuclear miR-9 and enter more frequently into cell cycle as shown by expression of PCNA (yellow arrow) when compared to cells that are electroporated with the control construct (top panel) which do display miR-9 in the nucleus (red asterisks). Scale bar=5µm. (**D**) ISH with miR-9 LNA probe (magenta) with fluorescent immunostaining of *gfap*:GFP (green) and DAPI nuclear counterstaining (dark blue) after ventricular injection of LMB (bottom panel) or a MeOH control (top panel). A noticeable increase in the number of cells with high miR-9 nuclear staining is observed. Scale Bar=20µm (**E**) Quantifications of the experiment shown in D showing the percentage of NSCs with nuclear miR-9 staining after MeOH or LMB intraventricular injections. n=3 brains per condition; data are represented as mean ± 95% CI. (**) p<0.01; one-way ANOVA with Bonferroni post-hoc correction.

Figure S7. Expression of miR-9 in mouse neurogenic regions and controls of experiments on cultured mouse AH-NSCs, related to figure 6

(**A**) Representative images of miR-9 ISH on coronal sections of a 2 month-old mouse brain demonstrating expression in the neurogenic regions (SEZ-left panel and DG-right panel). Insets are higher magnification of area boxed in white. Scale bars=1000µm and 20 µm. (**B**) ISH with a control LNA probe on coronal sections of a 2 month-old mouse brain showing no signal, thus demonstrating the specificity of miR-9 ISH. (**C**) Representative high-magnification 2-dimensional image of the 10 month DG on the XY (top panels) and XZ (bottom panels) axes (yellow line = position of the XZ image) with Sox2 (light blue) and ki67 (green) immunofluorescence, miR-9 ISH (magenta) and a nuclear DAPI counterstain (grey) demonstrating that Sox2+Ki67+ (red arrow) activated NSCs do not have nuclear miR-9. Yellow arrow indicates a Sox2+Ki67- NSC with nuclear miR-9. Scale bars=5µm. (**D**, **E**) Immunofluorescence for MCM2 (**D**) and GFAP (**E**) on proliferating (left panels) and quiescent (right panels) adult hippocampal neural stem cells (AH-NSCs) demonstrating a decrease in MCM2 expression and a concomitant increase in GFAP expression in quiescent AH-NSCs. (**F**) Quantification of total levels of Ago2 by Western blot in three different samples of proliferating and quiescent AH-NSCs. Ago2 levels were normalized to beta-tubulin levels. Data are represented as mean ± 95% CI. No significant difference is observed between proliferating and quiescent NSCs.

Supplemental Tables

Table S1. Sequences of vivoMO used in this study, related to Experimental Procedures

vivoMO used in this study

name	sequence
miR-9 MO	TCATACAGCTAGATAACCAAAGA
processing MO1	CAGCTAGATAACCAAAGATAACA
processing MO6	GCTAGATAACCAAAGATAGCAACTA
control MO	AATGCTCAAGTTGCTTCTCAGATCC

Table S2. ISH probes used in this study, related to Experimental Procedures

List of ISH probes used in this study

RNA probes

gene	reference	T°C
gata3	*Neave et al., 1995*	65°C
her4	*Takke et al., 1999*	65°C
notch3	*Westin and Lardelli, 1997*	65°C
nrarpa	*Lamar et al. 2001*	65°C
primiR-9-2	*Nepal et al., 2015*	65°C
primiR-9-6	*Nepal et al., 2015*	65°C

LNA probes for microRNAs

microRNA	probe sequence (5'-3')	manufacturer	T°C
miR-9-5p	TCATACAGCTAGATAACCAAAGA	Exiqon (#88078)	45°C
miR-9-3p	ACTTTCGGTTATCTAGCTTTAT	Exiqon (#35178)	45°C
miR-128	AAAAGAGACCGGTTCACTGTGA	Exiqon (#35102)	53°C
let-7b	AACCACACAACCTACTACCTCA	Exiqon (#38001)	53°C
scramble miR	GTGTAACACGTCTATACGCCCA	Exiqon (#99004)	55°C
miR-9-5p	DIG-lTmCmAlTmAmClAmGmClTmAmGlAmUmAlAmCmClAmAmAlGlA	Ribotask	70°C
control probe	DIG-mGlTmGmUlAmAmClAmCmGlTmCmUlAmUmAiCmGmCiCmCmA	Ribotask	70°C

Table S3. Primary antibodies used in this study, related to Experimental Procedures

Primary antibodies used in this study			
Name	**Host**	**Antibody reference**	**Working concentration**
anti-Ago2	rat	Sigma (SAB4200085)	1:200 (ICC) 1:2000 (WB)
anti-Ago2/eIF2c2	mouse	Abcam (ab57113)	1:500 (IHC) 1:1000 (WB)
anti-BrdU	rat	Abcam (ab6326)	1:250 (IHC)
anti-cleaved caspase 3	rabbit	Cell signalling (9661)	1:500 (IHC)
anti-DDX6	rabbit	Euromedex (A300-460A)	1:2000 (WB)
anti-DIG	mouse	Roche (11333062910)	1:500 (ICC)
anti-fish leukocytes (4C4)	mouse	ECACC (92092321)	1:500 (IHC)
anti-FLAG	rabbit	Sigma (F7425)	1:500 (IHC) 1:5000 (WB)
anti-FLAG	mouse	Sigma (F1802)	1:1000 (WB)
anti-GFAP	rat	Invitrogen (13-0300)	1:500 (IHC,ICC)
anti-GFAP	rabbit	DAKO (Z0334)	1:500 (IHC,ICC)
anti-GFP	chicken	Aves Laboratories (GFP 1020)	1:1000 (IHC) 1:2000 (WB)
anti-GS	mouse	Millipore (MAB302)	1:1000 (IHC)
anti-Hu	human	gift from B. Zalc, Salpetrière hospital, Paris	1:2000 (IHC)
anti-Ki67	rabbit	Leica biosystems (NCL-ki67p)	1:200 (IHC)
anti-MCM2	rabbit	Abcam (ab4461)	1:500 (IHC)
anti-MCM5	rabbit	gift from S. Ryu (Ryu et al., 2005)	1:500 (IHC)
anti-panAgo	mouse	Millipore (MABE56)	1:100 (IHC) 1:200 (WB)
anti-PCNA	rabbit	Genetex (GTX124496)	1:500 (IHC)
anti-PCNA	mouse	Santa Cruz (SC56)	1:250 (IHC)
anti-pH3	rabbit	Millipore (06-570)	1:2000 (WB)
anti-Sox2	mouse	Abcam (ab171380)	1:200 (IHC)
anti-Sox2	rabbit	Abcam (ab97959)	1:2000 (WB)
anti-βtubulin	rabbit	Abcam (ab6046)	1:2000 (WB)

IHC: Immunohistochemistry
ICC: Immunocytochemistry on mouse cells
WB: Western blot

Table S4. Primers used in this study, related to Experimental Procedures

qPCR Primers	
transcript	**primer**
primiR-9-1	F-CTGGTTGGATGGAAATGGAC R-GGAGACTTGGGAGGGAAAAG
primiR-9-2	F-GCTCTCCTCTGGTGACTTTT R-GCAATGCTCCATACGTTGCT
primiR-9-3	F-CAGTGGGGCCTAATCATCTC R-TTGCTTTTCTCTTGCTGTCTTC
primiR-9-4	F-GCAATAGCTCCATGTGACCA R-CCTCGTTCCAATTCAAAGC
primiR-9-5	F-TGTTTTAGCAACTTCTCCACTTG R-GCATCTTCGTGTCAATAGGC
primiR-9-6	F-CCCTGTTTTCGTTTATCAGGTC R-CAGATTCCCTGCGATCATT
primiR-9-7	F-GACCAAACAAACACTGACTCCA R-TCTCCGCTGCTCGGCTCT
her4	F-AGTCACATCTGGAGACCTG R-TGATCACATCGTCACTGAACA
gapdh	F-TCTTCTGTGTGGCGGTGTAG R-AACTTTGGTATTGAGGAGGCTCT
β-*actin*	F-AAGGCCAACAGGGAAAAGAT R-GTGGTACGACCAGAGGCATA
U2	F-ATCTGATACGTGCCCTACCC R-TACTGCAATACCGGGTCGAT
Primers used for cloning	
gene	**primers**
tnrc6a	F-TATGAATTCTAACCGAAGGAGGGGTAATCAG
	R-TATCTCGAGTCATCCAGCAGTGTTCTTGTTCC
ago2	F-TTTCTCGAGATGTATCCCATTGGAGCAGC
	R-TTTTCTAGAGGCTTGGTTCTGGCTTTGT

Supplemental Experimental Procedures

Construction of expression constructs

The fragment encoding the highly conserved zebrafish tnrc6a GW-I/II was amplified from adult brains cDNAs using the Expand High Fidelity PCR system (Roche). The PCR fragment was cloned into the pME-eGFP no stop vector of the Tol2kit (Kwan et al., 2007) using EcoRI and XhoI restriction sites. The dn-tnrc6-gfp fusion gene was then placed downstream of the previously identified her4 promoter (Yeo et al., 2007) or CMV/SP6 (for mRNA synthesis) by performing a gateway LR reaction (Invitrogen) using the p5E-her4, p5E-CMV/SP6 (Tol2kit), pME-eGFP-dn-tnrc6, p3E-polyA (Tol2kit) and pDest-Tol2pA2 (Tol2kit) entry vectors. The full length zebrafish ago2 was amplified from adult brains cDNAs using the Phusion High Fidelity PCR kit (Thermo Scientific). The PCR fragment was cloned into the pCS2+Flag plasmid (Peter Klein Lab, Addgene) using XhoI and Xbal restriction sites. All primers used are listed in table S4.

Sensor assays

To obtain sensor constructs, 3' entry plasmids harboring 10 bulged binding sites for miR-9 (miR-9 sensor) or miR-218 (control sensor) were kindly provided by Jean Giacomotto (University of Sydney, Australia) and a gateway LR reaction using p5E-CMV/SP6, pME-mCherry and pDest-Tol2pA2 (Tol2kit) was performed. Capped mRNAs were synthetized using mMessage mMachine kit (Ambion). Embryos were injected with mRNA encoding mCherry and harboring 10 bulged binding sites for miR-9 (miR-9 sensor) or 10 bulged binding sites for miR-218 (control sensor) in their 3'UTR (50ng/µL), with or without miR-9 duplexes (10µM), as previously described (Leucht et al., 2008). Embryos were co-injected with GFP mRNA (50ng/µL) or DN-TNRC6-GFP mRNA (at increasing doses: 50ng/µL or 250ng/µL). Embryos were imaged at 24hpf using a fluorescent stereomicroscope.

Co-immunoprecipitation of proteins

Capped mRNAs of the different constructs were synthetized using mMessage mMachine kit (Ambion) and injected in one-cell stage embryos (50ng/µL). Injected embryos were dechorionated and deyolked at 24hpf in ice-cold embryo medium supplemented with proteases inhibitors (Roche) and samples were homogeneized in ice-cold lysis buffer (10mM Tris pH 7.5, 150mM NaCl, 0.5mM EDTA, 0.5% NP-40, protease inhibitors). Lysates were cleared by centrifugation at 12000g for 15 minutes at 4°C and incubated either with anti-FLAG M2 magnetic beads (Sigma) or GFP-TRAP magnetic beads (Chromotek) for 1 hour at 4°C. Beads were washed 3 times in wash buffer (10mM Tris pH7.5, 150mM NaCl, 0.5mM EDTA, protease inhibitors). Proteins were then dissociated from the magnetic beads by boiling the samples in SDS sample buffer and samples were analyzed by Western blotting.

Western Blot

Protein lysates were extracted from embryos and adult telencephali. Embryonic lysates were prepared as described previously (Leucht et al., 2008). To prepare lysates from adult telencephali, brains were dissected on ice in the presence of protease inhibitors (Roche) and the telencephali were snap frozen in liquid nitrogen and homogenized in RIPA buffer. Protein lysates were diluted 1:1 in Laemmli buffer (Biorad) supplemented with β-mercaptoethanol and heated for 5 min at 95°C. For Western blots from AH-NSCs samples, cells were collected (1.2 million proliferating and 400,000 quiescent AH-NSCs per sample), boiled at 95°C for 5 min in SDS buffer and subsequently sonicated. To calibrate to cellular input, proliferating and quiescent cell lysates were diluted to a ratio of 1:3 prior to loading. Samples and the Kaleidoscope prestained ladder (Biorad) were loaded into mini-protean TGX precast gels (Biorad) and migrated for 40 min. at 200V in 10x Tris/Glycine/SDS buffer (Biorad). Gels were blotted onto an Invitrolon PVDF membrane (Life Technologies) at 15V for 30-60 min. Membranes were blocked in 5% non-fat dry milk (in PBT (PBS+0.1% tween-20)), incubated with primary antibodies (listed in table S3) overnight at 4°C, washed three times in PBT and subsequently incubated with secondary antibodies conjugated to HRP (1:20000, Thermo Scientific, 34082) for 1 at RT. After three washes in PBT and a brief incubation in Pierce chemiluminescence reagent (Thermo Fisher) detection was carried out using the myECL imager (Thermo Scientific) and band size and intensity analysis was done using the myImageAnalysis software (Thermo Fisher).

Cellular Fractionation of proteins and RNAs

The separation and preparation of cytoplasmic, membrane, nuclear soluble, chromatin-bound and cytoskeletal protein extracts was performed with the Subcellular Protein Fractionation Kit for tissues (Thermo Scientific, #87790) according to manufacturer's instructions, starting from 40 adult telencephali (~200mg of tissue) dissected in sterile ice cold PBS. Cytoplasmic and nuclear tissue fractionation and RNA purification was carried out using the Cytoplasmic and Nuclear RNA purification Kit (Norgen Biotek Corp., #37400) according to manufacturer's instructions using either 6 adult telencephali per sample or 4 juvenile (1 month old) whole brains per sample. RT-PCR for gapdh and U2 was performed to verify the purity of the cytoplasmic and nuclear fractions using 18ng total RNA input and using the following reagents: Superscript II kit (Invitrogen) with Random Hexamer Primers (Thermo Scientific), GoTaq Green Master Mix (Promega, M712).

Supplemental References

Kwan, K.M., Fujimoto, E., Grabher, C., Mangum, B.D., Hardy, M.E., Campbell, D.S., Parant, J.M., Yost, H.J., Kanki, J.P., and Chien, C.-B. (2007). The Tol2kit: a multisite gateway-based construction kit for Tol2 transposon transgenesis constructs. Dev. Dyn. 236, 3088–3099.

Lamar, E., Deblandre, G., Wettstein, D., Gawantka, V., Pollet, N., Niehrs, C., and Kintner, C. (2001). Nrarp is a novel intracellular component of the Notch signaling pathway. Genes Dev. 15, 1885–1899.

Neave, B., Rodaway, A., Wilson, S.W., Patient, R., and Holder, N. (1995). Expression of zebrafish GATA 3 (gta3) during gastrulation and neurulation suggests a role in the specification of cell fate. Mechanisms of Development 51, 169–182.

Nepal, C., Coolen, M., Hadzhiev, Y., Cussigh, D., Mydel, P., Steen, V.M., Carninci, P., Andersen, J.B., Bally-Cuif, L., Müller, F., et al. (2015). Transcriptional, post-transcriptional and chromatin-associated regulation of pri-miRNAs, pre-miRNAs and moRNAs. Nucleic Acids Res.

Ryu, S., Holzschuh, J., Erhardt, S., Ettl, A.-K., and Driever, W. (2005). Depletion of minichromosome maintenance protein 5 in the zebrafish retina causes cell-cycle defect and apoptosis. Proc. Natl. Acad. Sci. U.S.A. 102, 18467–18472.

Westin, J., and Lardelli, M. (1997). Three novel Notch genes in zebrafish: implications for vertebrate Notch gene evolution and function. Dev Gene Evol 207, 51–63.